Transient core surface dynamics from ground and satellite geomagnetic data

M Istas, Nicolas Gillet, C C Finlay, M D Hammer, L Huder

Geophysical Journal International

Geophys. J. Int. (2023) **233,** 1890–1915 https://doi.org/10.1093/gji/ggad039
Advance Access publication 2023 January 31
GJI Geomagnetism, Rock Magnetism and Palaeomagnetism

Transient core surface dynamics from ground and satellite geomagnetic data

M. Istas,[1] N. Gillet,[1] C. C. Finlay,[2] M. D. Hammer[2] and L. Huder[3]

[1] *Univ. Grenoble Alpes, Univ. Savoie Mont Blanc, CNRS, IRD, UGE, ISTerre,*38000 *Grenoble, France. E-mail: Nicolas.Gillet@univ-grenoble-alpes.fr*
[2] *Division of Geomagnetism, DTU Space, Technical University of Denmark, Elektrovej* 327, 2800, *Kongens Lyngby, Denmark*
[3] *ESRF, 71 Av. des Martyrs, CS* 40220, 38043, *Grenoble, France*

Accepted 2023 January 20. Received 2023 January 20; in original form 2022 July 8

SUMMARY

We present an update of the geomagnetic data assimilation tool pygeodyn, use it to analyse ground and satellite-based geomagnetic data sets, and report new findings on the dynamics of the Earth's outer core on interannual to decadal timescales. Our results support the idea that quasi-geostrophic Magneto-Coriolis waves, recently discovered at a period of 7 yr, also operate on both shorter and longer timescales, specifically in period bands centred around 3.5 and 15 yr. We revisit the source of interannual variations in the length of day and argue that both geostrophic torsional Alfvén waves and quasi-geostrophic Magneto-Coriolis waves can possibly contribute to spectral lines that have been isolated around 8.5 and 6 yr. A significant improvement to our ensemble Kalman filter algorithm comes from accounting for cross-correlations between variables of the state vector forecast, using the 'Graphical lasso' method to help stabilize the correlation matrices. This allows us to avoid spurious shrinkage of the model uncertainties while (i) conserving important information contained in off-diagonal elements of the forecast covariance matrix, and (ii) considering a limited number of realizations, thus reducing the computational cost. Our updated scheme also permits us to use observations either in the form of Gauss coefficient data or more directly as ground-based and satellite-based virtual observatory series. It is thanks to these advances that we are able to place global constraints on core dynamics even at short periods.

Key words: Earth rotation variations; Satellite magnetics; Inverse theory; Core.

1 INTRODUCTION

1.1 Transient dynamics within the Earth's core

The present era of geomagnetic field monitoring from space now covers more than two decades. This large amount of observational data enables the study of fine details of the changes in space and time of the field that originates in Earth's core, which in turn provides new details concerning the dynamics taking place within the liquid iron core (Lesur *et al.* 2022). A new framework for interpreting the observed field changes and the underlying core motions has been recently brought to the fore by Gillet *et al.* (2022), based on quasi-geostrophic (QG) Magneto-Coriolis (MC) waves. It favours motions parallel to the equatorial plane that are invariant along the Earth's rotation axis due to the predominance of the Coriolis force. MC waves are sustained by both the Coriolis and the Lorentz forces, and are thus sensitive to the background magnetic field within the core.

QG MC waves were first described analytically by Hide (1966), and have been the subject of a large number of theoretical and numerical studies (e.g. Canet *et al.* 2014; Hori *et al.* 2018). They have long been believed to play an important role for centennial and longer field changes. However, Gerick *et al.* (2021) recently pointed out the existence of interannual QG MC eigenmodes possessing large azimuthal length-scales that are accessible to observations. Furthermore, the footprint of such waves turns out to be easier to detect towards the equator because, at low latitudes, a short wavelength in the cylindrical radial direction translates into a much larger meridional length-scale on the spherical core surface where we study the dynamics. Gillet *et al.* (2022) recently reported the detection of such QG MC waves at interannual periods based on flows derived from the CHAOS-7 field model covering the satellite era (Finlay *et al.* 2020). They found waves dominated by long length-scales in the azimuthal direction (predominantly of azimuthal wavenumber $m = 2$), and significantly shorter length-scales

along the cylindrical radius, with a period close to 7 yr. Since QG MC waves are highly dispersive, one can envision their existence at other periods with little modification of their wavelengths. The above description is consistent with analyses from recent dynamo simulations (Aubert & Gillet 2021), where similar such waves have been isolated (Gillet *et al.* 2022; Aubert *et al.* 2022). There, they seem to morph from QG Alfvén waves (for which the restoring force is only magnetic, see Aubert & Finlay 2019) excited deep in the core by convecting plumes.

1.2 Geomagnetic data assimilation

This interpretation of observed field changes in terms of core physics can be pursued by means of geomagnetic data assimilation algorithms, that target an inference of the core state while considering both observational and dynamical constraints (Fournier *et al.* 2010; Gillet 2019; Sanchez *et al.* 2019). However, we face several major difficulties in this quest. Dynamical models of the core based on the primitive equations, although they are now in a position to capture the physics at work in the core, still struggle to fully replicate interannual timescales in an operational manner (Aubert 2018; Aubert & Gillet 2021). On the observational side, the separation of the signal generated in the core from that associated with external (ionospheric and magnetospheric) sources is very challenging at periods approaching $\sim$1 yr (Finlay *et al.* 2017; Lesur *et al.* 2022).

This state of affairs has led to simplified approaches to geomagnetic data assimilation based either on advection by core surface flows (e.g. Whaler & Beggan 2015; Beggan & Whaler 2018), or to the use of dynamo models in a regime where rapid dynamics are not captured (e.g. Fournier *et al.* 2015; Sanchez *et al.* 2020). For a review in the context of IGRF models, see Fournier *et al.* (2021). Most of these approaches are based on Kalman filter or ensemble Kalman filter (EnKF) algorithms (Evensen 2003), which enable one to consider nonlinear dynamics. Although geodynamo model based schemes can be used to tentatively forecast decadal changes (Aubert 2015), they suffer from abrupt adjustments, triggering spurious transient responses that do not correspond to observed variations—even though this effect can be partly mitigated, see Aubert (2020). On the other hand, previous attempts at extracting, from noisy observations, rapid core flow changes based on simplified models of core surface dynamics have often suffered from spurious high frequency content (Beggan *et al.* 2009; Barrois *et al.* 2018).

The `pygeodyn` tool for assimilating magnetic observations (Huder *et al.* 2019) has been developed with the aim of avoiding the limitations of dynamo models at short timescales, while benefiting from their rich spatiotemporal dynamics on longer timescales. This is achieved by fitting parameters of a reduced stochastic model of the core surface evolution to time-series produced by numerical geodynamo models (Gillet *et al.* 2019). However, up to now, the observations assimilated into the `pygeodyn` scheme have consisted of Gauss coefficients from magnetic field models, at least in an operational context. Magnetic data collected above the Earth's surface with ground or satellite observatories had only been considered in a prototype application where, due to a coarse estimate of the forecast statistics, the irregular sampling of noisy observations generated unphysical rapid flow changes (Barrois *et al.* 2018). We present here an update of the `pygeodyn` tool including significant improvements in order to reduce the impact of noise, whether it be associated with non-Gaussian distribution of errors in geomagnetic data, or with noisy second-order statistics such as those constructed empirically based on a finite ensemble size. Regarding this latter issue, we adopt the Graphical lasso (G-LASSO) method (Friedman *et al.* 2007) in order to improve the estimation of the forecast covariance matrices that enter the EnKF at the heart of our software. The new algorithm is first applied to the COV-OBS-x2 field model (Huder *et al.* 2020), starting from 1880, which then sets the initial condition for the remainder of the reanalysis, starting from 1997, based on geomagnetic data collected at ground-based observatories (GGO) and on board of satellites, in the form of geomagnetic virtual observatory (GVO) data (Hammer *et al.* 2021b) which we use up to 2022. The GVO data format is well suited to a sequential assimilation tool such as `pygeodyn`.

Based on this reanalysis, performed using our updated version of `pygeodyn`, we obtain a new and extended estimate of core surface flow changes. Both zonal and non-zonal motions are analysed within the framework of the hydromagnetic waves recently proposed by Gillet *et al.* (2022) to interpret the observed interannual field changes (which includes secular acceleration pulses, see Chulliat & Maus 2014; Finlay *et al.* 2016). The non-axisymmetric wave with 7 yr period previously documented by Gillet *et al.* (2022) is not the fundamental mode, and QG MC waves likely exist on longer, and possibly shorter, periods. We investigate the existence of such QG MC waves and their potential link with the evolution of axisymmetric motions and thus with recorded fluctuations in the length-of-day (LOD). Such a link would provide a rationale for the synchronicity of LOD changes and geomagnetic jerks, reported from both geophysical observations (Holme & De Viron 2013; Duan & Huang 2020) and geodynamo simulations (Aubert & Finlay 2019; Aubert *et al.* 2022).

The result of our reanalysis also includes, in addition to a core surface flow model, a new time-dependent model of the geomagnetic field originating in Earth's core. This by-product constitutes an alternative to regularized field models such as CHAOS-7 (Finlay *et al.* 2020), or to models based on stochastic equations and a Kalman filter but not related to core surface flows such as the Kalmag (Baerenzung *et al.* 2020) or MCM (Ropp *et al.* 2020) models.

The paper is organized as follows: in Section 2 we present the geophysical (geomagnetic and geodetic) observations considered. Improvements to the `pygeodyn` assimilation tool and their effects are described in Section 3, where in particular we discuss why and how we implement an improved estimate of the forecast covariance matrix (§3.3.3–3.3.5). In Section 3.4 we present the magnetic field evolution recovered over the satellite era, while in Section 4 we document the interannual and decadal flow changes resulting from our reanalysis, together with their predictions to interannual changes in the LOD. We discuss the implications of our findings in Section 5.

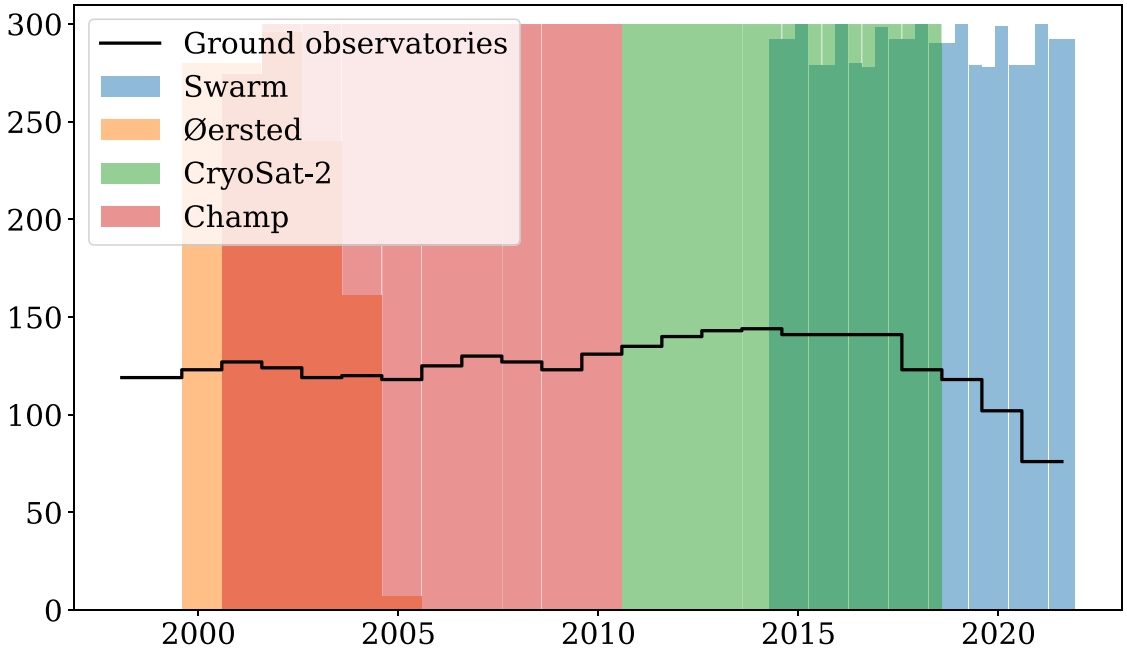

Figure 1. Number of observations available as function of time, where each count corresponds to an estimation of the vector magnetic field in the r, θ and ϕ components. The ground and virtual observatories are indicated as a continuous line or as histograms. At each assimilation step, all the available observations are used.

2 GEOPHYSICAL OBSERVATIONS

2.1 Geomagnetic ground-based observatories (GGO)

We make use of magnetic field time-series at 206 geomagnetic ground-based observatories that cover the period 1997–2021. These were derived from hourly mean values taken from the BGS database, version 0129, using Intermagnet and WDC Edinburgh data as available in 2022 February. The observatory data have been checked and corrected for known baseline jumps (Macmillan & Olsen 2013). Revised annual means were produced from hourly values using the procedure described by Olsen *et al.* (2014) for producing observatory revised monthly means, but by applying it to annual rather than monthly time windows. Estimates of the large-scale magnetospheric field and the solar-quiet ionospheric field (along with estimates of their Earth induced contributions) from the CHAOS-7.9 model (Finlay *et al.* 2020), and the CM4 (Sabaka *et al.* 2013) models respectively are first removed from the hourly mean observatory data. Then robust (Huber weighted) annual mean values are computed using an iterative reweighting procedure. To avoid offsets due to crustal biases we removed from each series the median difference between each GGO series and CHAOS-7.9 model estimates. Secular variation (SV) estimates were computed using first differences of the annual means. For each series considered individually, annual mean main field (MF) data are provided together with an uncertainty level $\sigma_{\rm obs}$, based on the robust (Huber weighted) r.m.s. difference to the CHAOS-7 field model for each series. Error variances on the SV data (in $(\mathrm{nT\,yr^{-1}})^2$) are then obtained as $\sigma^2_{\rm SV} = 2\sigma^2_{\rm obs}/\Delta t^2$, with $\Delta t = 1$ yr. These may in some locations/components appear conservative in comparison with error estimates derived directly on annual differences. In order to work with synchronized MF and SV data, we considered a two-point mean of the MF data, and thus consider for MF error variances $\sigma^2_{\rm MF} = \sigma^2_{\rm obs}/2$ (in nT^2). The temporal distribution of the resulting GGO data set used in this study is shown in Fig. 1.

2.2 Geomagnetic virtual observatories (GVO)

In addition to ground data we make use of a satellite-based Geomagnetic Virtual Observatories data set that consists of time-series of the magnetic field vector components together with its first time derivative (Mandea & Olsen 2006; Olsen & Mandea 2007; Hammer *et al.* 2021a) using either annual or 4-monthly sampling. The GVO series are provided at fixed points in space at satellite altitude. For each series satellite magnetic vector field measurements from within a local region defined by a cylinder of radius 700 km are used to compute a field estimate at a central target point during a specified time window. Here, we use a network of 300 globally distributed GVOs, created using the partitioning algorithm of Leopardi (2006). The GVOs were derived using the processing algorithm described in Hammer *et al.* (2021a), which has showed good agreement with magnetic records from ground observatory series during reference tests. We used only data from geomagnetically quiet and dark conditions. In order to reduce contributions from non-core field sources, in a similar fashion as for the GGO processing, the GVO algorithm removes estimates of the large-scale magnetospheric and ionospheric fields (along with estimates of their Earth-induced contributions) using the CHAOS-7.9 (Finlay *et al.* 2020), and CIY4 (Sabaka *et al.* 2018) models, respectively. To mitigate the biases due to the lithospheric field the field estimates from the LCS-1 model (Olsen *et al.* 2017) were also removed.

In this study, we have made use of GVO series derived from vector magnetic field measurements collected by the following satellite missions (see Fig. 1): the Ørsted mission (1999–2005 for vector field measurements), the CHAMP mission (2000–2010), calibrated platform magnetometer data from the CryoSat-2 mission (2010–2018) (Olsen *et al.* 2020), and also Level 1b MAG-L data, version 0505/0506, from the *Swarm* trio of satellites (2013–2022). Due to different orbital configuration of the upper satellite and lower pair, the local time (LT) coverage of the *Swarm* mission enables a 4-month time window to be used when computing the GVO estimates (Hammer *et al.* 2021a), whereas for the other missions it was necessary to use a 12-month time window in order to minimize problems associated with insufficient LT coverage. SV estimates for the first time derivative of the field were computed in all cases using annual differences. In order to work with synchronized MF and SV data, we considered a two-point mean of the MF data. Simple uncertainty estimates $\sigma_{\rm obs}$ for each GVO MF series were adopted, assuming the data errors to be time-independent and spatially uncorrelated—for more details see Hammer *et al.* (2021a). As for GGO data, SV error variances are then obtained as $\sigma^2_{\rm SV} = 2\sigma^2_{\rm obs}/\Delta t^2$—with $\Delta t = 1$ yr—and MF error variances are $\sigma^2_{\rm MF} = \sigma^2_{\rm obs}/2$.

2.3 COV-OBS-x2 field model

In addition to the geomagnetic observatory and satellite data described above, for the early part of our assimilation model (before 1997) we used the COV-OBS-x2 geomagnetic field model (Huder *et al.* 2020), starting from 1880. During this period the COV-OBS-x2 model relied primarily on ground observatory annual means, along with data from the POGO satellites (1965–1971) the MAGSAT satellite (1979–1980) and the DE-2 satellite (1981–1983), as well as ground and marine survey data (Gillet *et al.* 2013). COV-OBS-x2 is a time-dependent spherical harmonic field model with truncation degree 14 and using cubic B-spline basis with 2 yr knots in time. We also made use of the diagonal part of the model covariance matrix supplied along COV-OBS-x2. For further details on the COV-OBS-x2 model see Gillet *et al.* (2013) and Huder *et al.* (2020).

2.4 Length-of-day (LOD) records

We consider observations of the length-of-day over the period 1880–2022. For this purpose we have concatenated two data sets. For the most recent epochs (from 1962 onwards) LOD series are derived from VLBI (very large based interferometry) data. We use the C04 series (Bizouard & Gambis 2009), which have been cleaned for solid tides (the IERS 2000 model) and from atmospheric angular momentum contributions (Dobslaw *et al.* 2010). For the older times we make use of the Lunar97 series (Gross 2001), constrained by lunar eclipses. The two series have been concatenated by imposing the same average over the overlapping era. We finally removed from the resulting series a linear 1.78 ms per cy trend, to account for the mean trend observed over the past millenia (Stephenson *et al.* 2016).

3 A GEOMAGNETIC DATA ASSIMILATION ALGORITHM

3.1 Some prerequisite notations

We describe the time evolution of the core surface state vector using an Ensemble Kalman filter algorithm (Evensen 2003). It consists of a series of forecast (time-stepping a forward dynamical model) and analysis (regression of the model state when observations are available) steps, for an ensemble of N_e realizations, as described below. Let us consider a quantity (MF, flow, SV, etc.) represented by a vector $\mathbf{x}$. For any such vector, the statistical expectation is denoted $\mathbb{E}[\mathbf{x}] = \langle \mathbf{x} \rangle$, and the deviation from the expected value is $\delta \mathbf{x} = \mathbf{x} - \langle \mathbf{x} \rangle$. Let us now consider two quantities represented by vectors $\mathbf{x}$ and $\mathbf{y}$. The cross-covariance matrix between these two vectors is $P_{xy} = \mathbb{E}\left[\delta \mathbf{x} \delta \mathbf{y}^T\right]$, and

$$C_{xy} = \mathrm{diag}(P_{xx})^{-1/2} P_{xy} \mathrm{diag}(P_{yy})^{-1/2} \tag{1}$$

denotes the associated cross-correlation matrix. These may be estimated empirically from an ensemble of finite size. In this case $\tilde{P}_{xy}$ refers to the empirical (or sample) estimate of P_{xy}, obtained from an ensemble of N_e realizations $\left\{\mathbf{x}^j, \mathbf{y}^j\right\}_{j \in [1 \ldots N_e]}$ as

$$\tilde{P}_{xy} = \frac{1}{N_e - 1} \sum_{j=1}^{N_e} \delta \mathbf{x}^j \delta \mathbf{y}^{j\,T}. \tag{2}$$

The associated sample correlation matrix is then $\tilde{C}_{xy} = \mathrm{diag}(\tilde{P}_{xx})^{-1/2} \tilde{P}_{xy} \mathrm{diag}(\tilde{P}_{yy})^{-1/2}$. Throughout this paper, we denote by respectively $\mathbf{x}^f$ and $\mathbf{x}^a$ the forecasted and analysed vectors. The associated covariance matrices are noted $\tilde{P}^f_{xx}$ and $\tilde{P}^a_{xx}$, with similar notations for the correlation matrices.

3.2 Forward model of the core surface dynamics

Throughout we use the spherical coordinate system, of unit vectors $(\mathbf{1}_r, \mathbf{1}_\theta, \mathbf{1}_\phi)$ in the radial, meridional and azimuthal directions. We recall here the main characteristics of the forward model; in this regard we follow the approach of Gillet *et al.* (2019), to which we refer for

further details. The temporal evolution of the radial magnetic field is described by the radial part of the induction equation at the core–mantle boundary (CMB),

$$\frac{\partial B_r}{\partial t} = -\nabla_h \cdot (\mathbf{u}_h B_r) + \eta \nabla^2 B_r \,, \tag{3}$$

where B_r is the radial magnetic field at the core surface, η is the magnetic diffusivity and $\mathbf{u}_h$ the horizontal velocity field. B_r and $\mathbf{u}_h$ are parametrized in the spectral domain, by means of spherical harmonics. Above the core surface of radius $r_C = 3485$ km, the magnetic field is described by a potential, that is $\mathbf{B} = -\nabla V$, with

$$V\,(r > r_C, \theta, \phi) = r_E \sum_{n=1}^{n_b} \left(\frac{r_E}{r}\right)^{n+1} \sum_{m=0}^{n} \left(g_n^m \cos(m\phi) + h_n^m \sin(m\phi)\right) P_n^m(\cos\theta)\,. \tag{4}$$

$r_E = 6371.2$ km is the Earth's reference radius. g_n^m and h_n^m (in nT) are the Gauss coefficients of degree n and order m, P_n^m the Schmidt seminormalized Legendre functions, and n_b is the truncation degree for the magnetic field. The core surface flow is represented as (e.g. Holme 2015)

$$\mathbf{u}_h(\theta, \phi) = \nabla \times (Tr\mathbf{1}_r) + \nabla_h(rS)\,, \tag{5}$$

with T and S, respectively, the toroidal and poloidal scalars, which we decompose as

$$\begin{cases} T(\theta,\phi) = \displaystyle\sum_{n=1}^{n_u}\sum_{m=0}^{n} \left[t_{c_n}^m \cos(m\phi) + t_{s_n}^m \sin(m\phi)\right] P_n^m(\cos\theta) \\ S(\theta,\phi) = \displaystyle\sum_{n=1}^{n_u}\sum_{m=0}^{n} \left[s_{c_n}^m \cos(m\phi) + s_{s_n}^m \sin(m\phi)\right] P_n^m(\cos\theta) \end{cases}. \tag{6}$$

n_u is the truncation degree for the core surface flow, and t_{c,s_n}^m and s_{c,s_n}^m are the toroidal and poloidal spherical harmonic coefficients (in km yr^{-1}). The flow coefficients are then normalized as

$$\left(T_{c,s_n}^m, S_{c,s_n}^m\right) = \sqrt{\frac{n(n+1)}{(2n+1)}} \left(t_{c,s_n}^m, s_{c,s_n}^m\right)\,, \tag{7}$$

so that the core surface kinetic energy per harmonic degree n is

$$E_K(n) = \frac{1}{2}\rho \sum_m (T_{c,s_n}^m)^2 + (S_{c,s_n}^m)^2\,, \tag{8}$$

where $\rho = 10^4$ kg m^{-3} is the core density. At a given epoch, we store flow coefficients $(t_{c,s_n}^m, s_{c,s_n}^m)$ in a vector $\mathbf{u}$, and $(T_{c,s_n}^m, S_{c,s_n}^m)$ in a vector $\mathbf{U}$. Eq. (7) is then represented as $\mathbf{U} = N\mathbf{u}$ with N a diagonal normalization matrix. The flow is described up to spherical harmonic degree $n_u = 18$, so that the flow vectors $\mathbf{u}$ and $\mathbf{U}$ are of size $N_u = 2n_u(n_u + 2) = 720$.

Considering only the resolvable large length-scales of the fields (spherical harmonics of degrees $n \le n_b$ for the magnetic field and $n \le n_u$ for the flow, denoted by overlines), eq. (3) then transforms into

$$\frac{\partial \overline{B}_r}{\partial t} = -\overline{\nabla_h \cdot \left(\overline{\mathbf{u}}_h \overline{B}_r\right)} + e_r\,, \tag{9}$$

where the quantity e_r contains the errors of representativeness (with contributions from subgrid and diffusion processes). In matrix form this becomes

$$\dot{\mathbf{b}} = A(\mathbf{b})\mathbf{u} + \mathbf{e} = \mathbf{f} + \mathbf{e}\,, \tag{10}$$

where $\dot{\mathbf{b}}$, $\mathbf{b}$ and $\mathbf{e}$ store spherical harmonic coefficients for, respectively, the fields $\partial B_r/\partial t$, B_r and e_r (with a decomposition similar to eq. (4) for $\partial B_r/\partial t$ and e_r). Vectors $\dot{\mathbf{b}}$ and $\mathbf{e}$ are given in nT yr^{-1}. The MF, the SV and the error term are expanded up to $n_b = 13$, so that vectors for the MF, SV and error terms are each of size $N_b = n_b(n_b + 2) = 195$. The matrix $A(\mathbf{b})$, in nT km^{-1}, is of size $N_b \times N_u$.

The magnetic field evolution described by eq. (10) is coupled to a stochastic model for the flow and the error term (see below) that is anchored to statistics derived from time-series produced by a numerical model of the geodynamo. In contrast to Gillet *et al.* (2019), who used outputs from the *50p* numerical dynamo model of Aubert *et al.* (2017), we use here a time-series from the *71p* dynamo model (Aubert & Gillet 2021). The *71p* model involves dynamo control parameters closer to those expected for Earth, thus enabling a better separation of the turnover time in the core ($\tau_U = r_C/U \sim 130$ yr in both the Earth's core and the dynamo simulations, with U a typical core flow velocity) from the Alfvén time ($\tau_A = r_C/V_A \sim 2$ yr in the core, compared with 6 yr in *71p* and 15 yr in *50p*, with $V_A = B/\sqrt{\rho\mu}$ the Alfvén speed—B the typical field intensity deep in the core, $\mu = 4\pi 10^{-7}$ H m^{-1} its magnetic permeability).

In order to reduce the dimension of the flow state vector, $\mathbf{U}$ is projected onto a subspace of $N_v = 200$ components using a PCA. The PCA is based on a time-series of the core surface flow coefficients from the *71p* geodynamo model. Because of the strong spatial constraint brought by the rapid rotation of the Earth, using $N_v = 200$ components is enough to capture most of the geodynamo core surface kinetic energy (see Gillet *et al.* 2019). The flow vector is then represented as $\mathbf{u} = \langle\mathbf{u}\rangle + N^{-1}S\mathbf{v}$, with $\langle\mathbf{u}\rangle$ the background flow (averaged from snapshots of the

dynamo model extracted every $\Delta t^* = 10$ yr) and $\mathbf{v}$ the representation of the flow projected onto the principal components, with S a projection operator (e.g. Pais *et al.* 2015). eq. (10) then becomes

$$\dot{\mathbf{b}} = A(\mathbf{b})\langle \mathbf{u} \rangle + \tilde{A}(\mathbf{b})\mathbf{v} + \mathbf{e}\,, \tag{11}$$

where $\tilde{A}(\mathbf{b}) = A(\mathbf{b})N^{-1}S$ is a matrix of size $N_b \times N_v$ (in nT km^{-1}, since N and S are unitless). eq. (11) is then coupled to multivariate autoregressive stochastic equations of the order of 1 (AR-1) for $\mathbf{v}$ and $\mathbf{e}$:

$$\begin{cases} \mathrm{d}\mathbf{v} + D_v \mathbf{v}\mathrm{d}t & = \mathrm{d}\mathbf{w}_v \\ \mathrm{d}\mathbf{e} + D_e\left(\mathbf{e} - \langle \mathbf{e} \rangle\right)\mathrm{d}t & = \mathrm{d}\mathbf{w}_e \end{cases}. \tag{12}$$

The term $\langle \mathbf{e} \rangle$, similarly to $\langle \mathbf{u} \rangle$, is a time-averaged quantity derived from the geodynamo model time-series. $\mathbf{w}_{v,e}$ are multivariate Wiener processes. Their second-order statistics, as well as the drift matrices $D_{v,e}$, are derived following Gillet *et al.* (2019), based upon cross-covariances obtained here from time-series of the *71p* geodynamo model core surface states, sampled every 10 yr. The stochastic model (12) replicates the cross-covariances of the vectors $\mathbf{u}$ and $\mathbf{e}$ seen in the geodynamo simulation, as well as the main statistics of temporal increments in $\mathbf{u}$ and $\mathbf{e}$ (characterized by eigen-vectors and eigen-values of the drift operators $D_{v,e}$). The forward model is time-stepped using an explicit Euler scheme for the numerical integration of eq. (11) for the magnetic field, while an Euler–Maruyama scheme is used to time step the stochastic eq. (12) for the flow and the error term, using a time step $\Delta t^f = 1$ month.

3.3 Analysis

3.3.1 Model state and observation operators

At any epoch t where observations (either GGO, GVO or Gauss coefficients) are available, MF and SV data are stored in vectors $\mathbf{y}^o_{\mathrm{MF}}(t)$ and $\mathbf{y}^o_{\mathrm{SV}}(t)$, respectively. The analysis is then performed in two steps. The assimilation of MF data is done in a first step, from which we obtain an analysed state $\mathbf{b}^a(t)$. Then in a second step we assimilate SV data to get an analysis of the augmented state

$$\mathbf{z} = \left[\mathbf{v}^T, \mathbf{e}^T\right]^T\,, \tag{13}$$

of size $N_z = N_v + N_b$. MF data are linked to the model parameters stored in $\mathbf{b}$ by a linear observation operator H_b through

$$\mathbf{y}^o_{\mathrm{MF}} = H_b\mathbf{b} + \mathbf{e}^o_{\mathrm{MF}}\,. \tag{14}$$

$\mathbf{e}^o_{\mathrm{MF}}$ denotes the error vector on MF observations, whose cross-covariances are stored into a diagonal matrix R_{MF}. For Gauss coefficient data, H_b is simply the identity matrix of size n_b. For observations above the Earth's surface (GGO and/or GVO), analytical expressions for H_b can be found in Barrois *et al.* (2018), or more generally in Sabaka *et al.* (2010). Similarly SV data are related to $\dot{\mathbf{b}}$ by

$$\mathbf{y}^o_{\mathrm{SV}} = H_b\dot{\mathbf{b}} + \mathbf{e}^o_{\mathrm{SV}}\,. \tag{15}$$

$\mathbf{e}^o_{\mathrm{SV}}$ stands the error vector on SV observations, whose cross-covariances are stored into a diagonal matrix R_{SV}. Using relations (11) and (13), eq. (15) can be written

$$\Delta\mathbf{y}^o_{\mathrm{SV}} = \mathbf{y}^o_{\mathrm{SV}} - H_b A\left(\mathbf{b}^a\right)\langle \mathbf{u} \rangle = H_z\left(\mathbf{b}^a\right)\mathbf{z} + \mathbf{e}^o_{\mathrm{SV}}\,, \tag{16}$$

with the forward operator $H_z\left(\mathbf{b}^a\right) = \left[H_b\tilde{A}\left(\mathbf{b}^a\right) \mid H_b\right]$. This represents an extension, to observations made above Earth's surface, of the algorithm of Gillet *et al.* (2019) that was initially developed for data in the form of Gauss coefficients.

3.3.2 Analysis of MF and SV data in the presence of outliers

Due to the presence of remaining unmodelled external field signals in both GVO and GGO data, as well as outliers particular in the GVOs based on satellite platform magnetometer data, the distribution of data residuals is in practice not Gaussian. Gaussian data error statistics were implicitly assumed in our previous stochastic flow and field reconstructions using either GVO (Barrois *et al.* 2018) or Gauss coefficient (Gillet *et al.* 2019) data, via the use of a L_2 norm measure of the misfit to observations. As shown in Fig. 2, a Gaussian distribution is inconsistent with the long tails we find in the distributions of the normalized prediction errors from the ensemble average solution,

$$\epsilon_i = \left(y_i^o - \left\langle y_i^p \right\rangle\right)/\sigma_i^o\,. \tag{17}$$

The term y_i^p describes the model prediction to the ith observation y_i^o, with σ_i^o its associated uncertainty (see Section 2 for details), while brackets indicate the ensemble average. Use for instance of a L_1-norm for the data misfit would be more consistent with a long-tailed error distribution, but in this case one expects N observations to be fit exactly, where N is the number of unknowns (Walker & Jackson 2000). Since our number observations N^o is not much larger than the number of unknowns (N_b or N_z), we would then have a risk of overfitting the data. Instead, we assume a Huber probability distribution of normalized errors (e.g. Olsen 2002),

$$P_c(\epsilon) \propto \exp(-L_c(\epsilon))\,, \quad \text{with} \quad L_c(\epsilon) = \begin{cases} \epsilon^2/2 & \text{if } |\epsilon| < c \\ c|\epsilon| - c^2/2 & \text{if } |\epsilon| \geq c \end{cases} \tag{18}$$

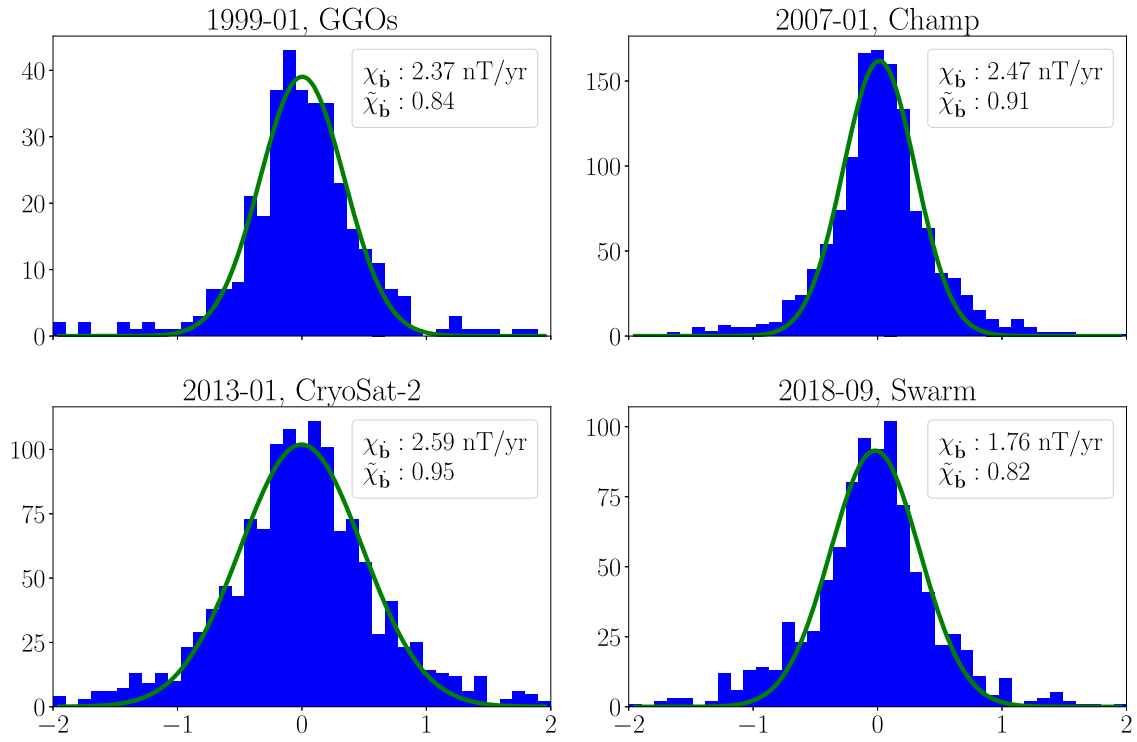

Figure 2. Histograms of the normalized residuals (as defined in eq. 17) averaged over all realizations from case $G^{0.1}_{400}$, at epochs 1999-01, 2007-01, 2013-01 and 2018-09. Histograms consider only observations from the ground observatories, CHAMP, CryoSat-2 and Swarm, respectively. The green curve is a fit of a Huber distribution to the distribution of residuals. The legends indicate the normalized and dimensional misfits (see eqs 25–26).

and the constant $c = 1.5$. In the following, we detail the algorithm used to recover the model parameters that, given noisy observations, maximize the probability of the residuals, as provided with eq. (18).

At each epoch t^a where GGO and/or GVO data are available, an ensemble $\left\{\mathbf{b}^{a,j}(t^a)\right\}_{j=1\ldots N_e}$ of analysed MF vectors are obtained using an iterative reweighted least-squares algorithm (Farquharson & Oldenburg 1998). To create the ensemble we perturb each datum y_i^o using, for the sake of simplicity, a Gaussian random variable within $N(0, \sigma_i^o)$. At each iterative step k, and for all ensemble members $j \in [0, N_e]$, one has

$$\mathbf{b}^{a,j}_{k+1} = \mathbf{b}^{f,j} + P^f_{bb} H_b^T \left(H_b P^f_{bb} H_b^T + \widetilde{R}_{\rm MF}\left(\mathbf{b}^{a,j}_k\right)\right)^{-1} \left(\mathbf{y}^{o,j}_{\rm MF} - H_b \mathbf{b}^{f,j}\right), \tag{19}$$

with $\widetilde{R}^{-1}_{\rm MF}(\mathbf{b}^{a,j}_k) = R^{-1/2}_{\rm MF} W_{\rm MF}(\mathbf{b}^{a,j}_k) R^{-1/2}_{\rm MF}$. The weight matrix $W_{\rm MF}$ is diagonal, with elements

$$W_{{\rm MF}ii}(\mathbf{b}^{a,j}_k) = \begin{cases} 1 & \text{if } |\epsilon_i\left(\mathbf{b}^{a,j}_k\right)| < c \\ c/|\epsilon_i\left(\mathbf{b}^{a,j}_k\right)| & \text{if } |\epsilon_i\left(\mathbf{b}^{a,j}_k\right)| \geq c \end{cases}, \text{ and } \epsilon\left(\mathbf{b}^{a,j}_k\right) = R^{-1/2}_{\rm MF}\left(\mathbf{y}^{o,j}_{\rm MF} - H_b \mathbf{b}^{a,j}_k\right). \tag{20}$$

$\left\{\mathbf{b}^{f,j}(t^a)\right\}_{j=1\ldots N_e}$ is the ensemble of forecast MF estimated at the analysis epoch, and

$$P^f_{bb}(t^a) = \mathbb{E}\left[\delta\mathbf{b}^f(t^a)\delta\mathbf{b}^f(t^a)^T\right] \tag{21}$$

is the associated forecast covariance matrix. It is approximated empirically from the ensemble of realizations, as described below in §3.3.4–3.3.5. We stop the iterative process when the relative change in the solution between two steps is less that 10^{-4}. In practice, performing 10 to 15 iterations of eq. (19) is enough to reach convergence. The iterative process for the analyses is computed separately for all ensemble members. It is initiated by setting $W_{\rm MF}$ equal to the identity matrix.

Once an ensemble $\left\{\mathbf{b}^{a,j}(t^a)\right\}_{j=1\ldots N_e}$ of analysed MF is obtained, an ensemble of analysed augmented state $\left\{\mathbf{z}^{a,j}(t^a)\right\}_{j=1\ldots N_e}$ is obtained by inverting the SV data using the same iterative algorithm,

$$\mathbf{z}^{a,j}_{k+1} = \mathbf{z}^{f,j} + P^f_{zz} H_z^{jT} \left(H_z^j P^f_{zz} H_z^{jT} + \widetilde{R}_{\rm SV}(\mathbf{z}^{a,j}_k)\right)^{-1} \left(\Delta\mathbf{y}^{o,j}_{\rm SV} - H_z \mathbf{z}^{f,j}\right), \tag{22}$$

with $\widetilde{R}^{-1}_{\rm SV}(\mathbf{z}^{a,j}_k) = R^{-1/2}_{\rm SV} W_{\rm SV}(\mathbf{z}^{a,j}_k) R^{-1/2}_{\rm SV}$ and $H_z^j = H_z\left(\mathbf{b}^{a,j}\right)$. The weight matrix $W_{\rm SV}$ is diagonal with elements

$$W_{{\rm SV}ii}\left(\mathbf{z}^{a,j}_k\right) = \begin{cases} 1 & \text{if } |\epsilon_i\left(\mathbf{z}^{a,j}_k\right)| < c \\ c/|\epsilon_i\left(\mathbf{z}^{a,j}_k\right)| & \text{if } |\epsilon_i\left(\mathbf{z}^{a,j}_k\right)| \geq c \end{cases}, \text{ and } \epsilon\left(\mathbf{z}^{a,j}_k\right) = R^{-1/2}_{\rm SV}\left(\Delta\mathbf{y}^{o,j}_{\rm SV} - H_z^j \mathbf{z}^{a,j}_k\right). \tag{23}$$

$\left\{\mathbf{z}^{f,j}(t^a)\right\}_{j=1...N_e}$ is the ensemble of forecast augmented state vectors estimated at the analysis epoch, and

$$P^f_{zz}(t^a) = \mathbb{E}\left[\delta\mathbf{z}^f(t^a)\delta\mathbf{z}^f(t^a)^T\right] \tag{24}$$

is the associated forecast covariance matrix. Below in §3.3.3–3.3.5 we show how we improve the estimation of matrices P^f_{bb} and P^f_{zz}, in comparison with the previous work of Gillet *et al.* (2019). The above iterative estimate based on Huber weights is only considered when inverting GGO/GVO data. A simple linear analysis is performed at epochs where the input data takes the form of Gauss coefficients.

Fig. 2 shows histograms of SV residuals $\epsilon(\mathbf{z}^{a,j})_{j\in[1,N_e]}$, at the end of the iterative process, of the CHAMP, CryoSat-2, *Swarm* and GGO data sets, respectively, at example epochs when these data were considered. It also reports the normalized misfit

$$\tilde{\chi}_{\dot{\mathbf{b}}} = \frac{1}{N^o N_e}\sum_{i=1}^{N^o}\sum_{j=1}^{N_e} L_c\left(\epsilon_i\left(\mathbf{z}^{a,j}\right)\right) \tag{25}$$

and the dimensional misfit

$$\chi_{\dot{\mathbf{b}}} = \frac{1}{N^o N_e}\sum_{i=1}^{N^o}\sum_{j=1}^{N_e} L_c\left(\sigma^o_i\epsilon_i\left(\mathbf{z}^{a,j}\right)\right)\,, \tag{26}$$

averaged over all GVO sites at these epochs. The median residuals in all cases indicate negligible biases, less than 0.05 in absolute value. Furthermore, the shape of the prediction error distributions shows that the reweighting algorithm accounts well for the presence of non-Gaussian tails. Normalized (Huber weighted) misfits are slightly below unity for all considered epochs, indicating that all data sets are adequately fit. Dimensional misfits show that our algorithm is able to predict annual GVO SV data within less than 2 nT yr^{-1} for *Swarm*. Misfits are larger for CHAMP and CryoSat-2, though in both cases less than 3 nT yr^{-1} in average. Such relatively low values can probably be attributed to the fact that we consider 12-monthly robust averages when building these GVO.

3.3.3 Limitations with previous estimates of the forecast covariance matrices

Up to now, in the `pygeodyn` software the matrix P^f_{bb} defined in eq. (21) had been considered time independent, and equal to P^*_{bb} the cross-covariance of the numerical geodynamo series employed to build the forward model (Gillet *et al.* 2019). This simplified set-up was considered, because for initial applications of the algorithm to Gauss coefficient data from the COV-OBS field model series, the result of the re-analysis was not found to be sensitive to this *a priori* choice. However, when considering GVO/GGO observations instead of Gauss coefficients, there are irregularities in the data sampling (for instance gaps due to the lack of observations from satellite missions at some times, or uneven data coverage associated with varying external conditions) that could possibly induce unphysical jumps in the recovered main field series. Indeed, under weak observational constraint and using a loose prior such as P^*_{bb}, coefficients in $\mathbf{b}^a$ are abruptly driven back towards the background state (here from the time average geodynamo). Such discontinuities in the MF can subsequently generate severe jumps in the reconstructed flow (as already witnessed in the prototype data assimilation scheme described by Barrois *et al.* 2018). In order to resolve such problems it is necessary to more carefully model the spread within the ensemble of forecast field states.

Furthermore, Gillet *et al.* (2019) had approximated P^f_{zz}, defined in eq. (24), from (i) the empirical spread within the ensemble of analysed states and (ii) analytical properties of the stochastic eqs (12) that describe the time evolution of $\mathbf{z}(t)$, while at the same time discarding all possible cross-covariances between $\delta\mathbf{e}^f$ and $\delta\mathbf{v}^f$ (or $P^f_{ev} = 0$). This pragmatic approach allowed sensible estimates of the diagonal elements of P^f_{zz}, and ensured the stability of the filter (the matrices were well conditioned in all situations). However, possibly important anticorrelations between $\delta\mathbf{e}^f$ and $\delta\mathbf{f}^f$ were ignored, as explained below—we recall that $\delta\mathbf{f} = \tilde{A}(\mathbf{b})\mathbf{v} - \left\langle\tilde{A}(\mathbf{b})\mathbf{v}\right\rangle$.

The spread within the ensemble of SV predictions at the forecast step ($\{\mathbf{y}^{f,j}\}_{j\in[1,N_e]}$, where $\mathbf{y}^{f,j} = \mathbf{e}^{f,j} + \mathbf{f}^{f,j}$), is provided by the diagonal of

$$P^f_{yy} = P^f_{ee} + P^f_{ff} + P^f_{ef} + P^f_{fe}\,. \tag{27}$$

If accurate observations and short timespans between two analyses are used, the dispersion within the ensemble of SV forecasts can be rather small. Meanwhile, the spread within the ensembles of realizations of both $\mathbf{e}^f$ and $\mathbf{f}^f$ is relatively larger, as many combinations of solutions to the inverse problem can reasonably fit the data. This implies

$$\mathrm{diag}\left(P^f_{yy}\right) \ll \mathrm{diag}\left(P^f_{ee}\right) + \mathrm{diag}\left(P^f_{ff}\right)\,, \tag{28}$$

and consequently the diagonal elements of P^f_{ef} must be negative, that is $\delta\mathbf{e}^f$ and $\delta\mathbf{f}^f$ have to be significantly anticorrelated. Furthermore, the spread within the ensemble $\{\mathbf{f}^{f,j}\}_{j\in[1,N_e]}$ is mainly due to the dispersion within the ensemble of flow solutions (as $\mathbf{b}$ is more directly constrained than $\mathbf{u}$, and its evolution smoother). This implies $P^f_{ef} \simeq P^f_{ev}A(\mathbf{b}^f)$, and consequently $P^f_{ev} \neq 0$. The anticorrelation between $\mathbf{e}$ and $\mathbf{f}$ appears clearly in Fig. 3(e), which shows sample correlation matrix (in the SV data domain) computed in a case with $N_e = 400$ realizations. This motivates the use of an algorithm capable of handling non-zero cross-covariances in P^f_{zz}, because neglecting significant cross-covariances within the ensemble of forecast state variables is known to produce biased inference of the vector state, and thus lose of part of the information carried by the data. We review in the Section 3.3.4 several possibilities from the literature for retaining cross-covariances, and describe in Section 3.3.5 the Graphical lasso (G-LASSO) approach that we have followed.

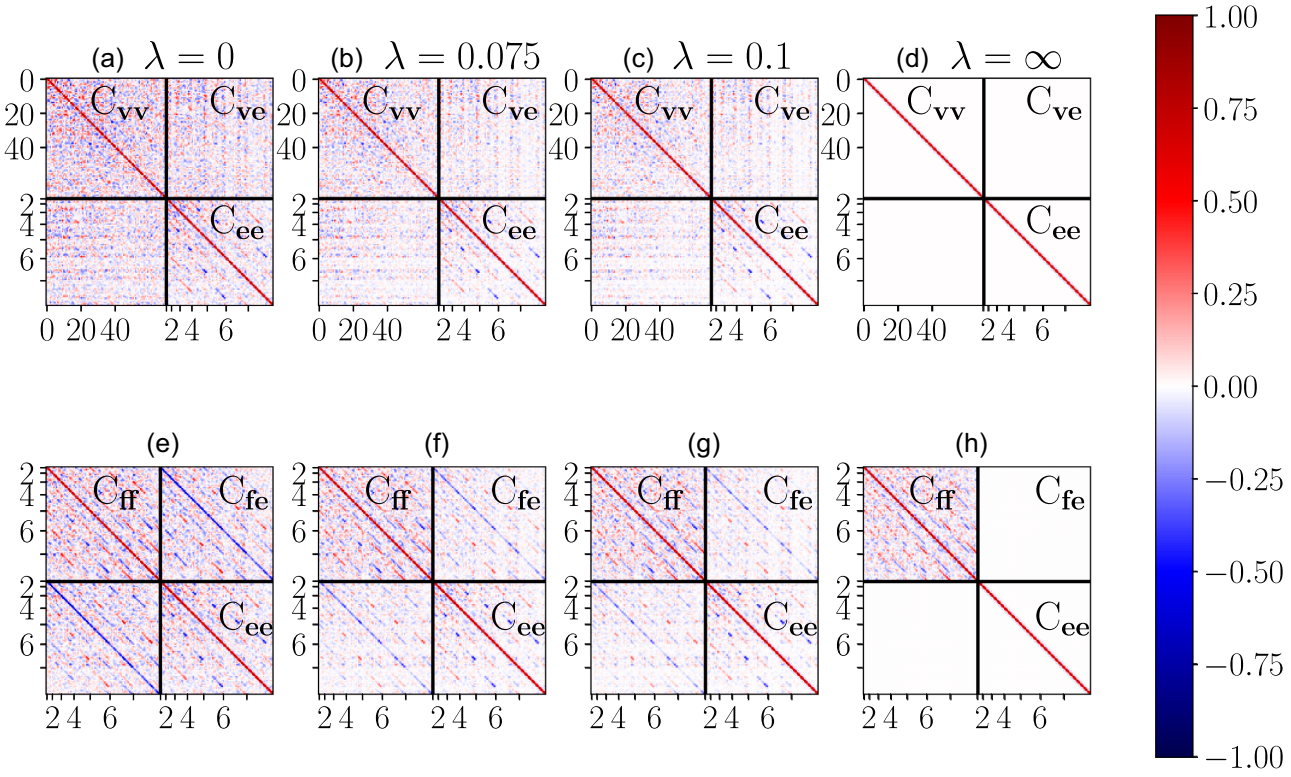

Figure 3. (a) and (e): Empirical forecast correlation matrices computed from 400 realizations, extracted from the reanalysis $G^{0.1}_{400}$ at epoch 2018-01 (just before an assimilation step). (b) to (d) and (f) to (h): Application of G-LASSO for different values of λ. The top row (a to d) corresponds to correlation matrices involving the flow (**v**, after rotation via the PCA) and subgrid error (**e**) basis. The bottom row (e to f) corresponds to correlation matrices involving **e** and **f** the induction from the large length-scale flow. Correlation matrices are shown for increasing values of the parameter λ from left to right: from $\lambda = 0$ (empirical matrix P^f_{zz}) in (a, e) to $\lambda = \infty$ (diagonal matrix P^f_{zz}) in (d, h). For the sake of clarity, we only present elements of the matrices for spherical harmonic degrees $n \leq 7$ for **e** and **f**, and the first 63 elements for **v**. For **e** and **f**, elements are stored as follows: $(n, m) = (1, 0), (1, 1), (1, -1), (2, 0), (2, 1), (2, -1), (2, 2), (2, -2), (3, 0). \ldots$

Table 1. Several set-up considered throughout the paper, where each reanalysis label contains a subscript for the number of realizations N_e and a superscript for the value of the parameter λ.

Case	Covariance matrices	Realizations	Data	λ
$W^{0.075}_{400}/W^{\infty}_{400}$	G-LASSO	400	Covobs (Gauss coeffs)	0.075/∞
D^{∞}_{200}	diagonal	200	GGO+GVO	∞
E^{0}_{100}/E^{0}_{400}	empirical	100/400	GGO+GVO	0
$G^{0.1}_{200}/G^{0.15}_{200}/G^{0.2}_{200}$	G-LASSO	200	GGO+GVO	0.1/0.15/0.2
$G^{0.075}_{400}/G^{0.1}_{400}$	G-LASSO	400	GGO+GVO	0.075/0.1

Before going further, we list here the various cases that have been investigated in this study. The main input parameters (data kind, ensemble size, G-LASSO parameter, etc.) are summarized in Table 1. We performed several reanalyses that cover the period [1997,2021], using as observations GGO and GVO data sets. Two free parameters have to be chosen: the ensemble size N_e and λ the trade-off parameter that enters the G-LASSO algorithm. These two are not independent the one from the other (see Section 3.3.5). Reanalyses carried out with $\lambda \in]0, \infty[$ will be referred to as '$G^{\lambda}_{N_e}$'. $\lambda = \infty$ is equivalent to using diagonal forecast matrices (cases denoted $D^{\infty}_{N_e}$), while $\lambda = 0$ comes back to using the sample estimates given by eq. (2), with no effect of G-LASSO (cases noted $E^{0}_{N_e}$). The initial conditions for all the experiments reported here were the result of a previous reanalysis of the COV-OBS-x2 Gauss coefficient data (Huder *et al.* 2020), starting from 1880, using $\Delta t^f = 4$ months and $\Delta t^a = 12$ months. These 'warm-up' cases are referred to as '$W^{\lambda}_{N_e}$'. Two different warm-up reanalyses have been considered, so that the inversion of GVO/GGO data computed with $\lambda \neq \infty$ (resp. $\lambda = \infty$) are started from a warm-up also computed with $\lambda \neq \infty$ (resp. $\lambda = \infty$). In this way, the initial condition of D^{∞}_{200} is given by the reanalysis W^{∞}_{400}, while for $G^{0.1}_{400}$ or $G^{0.2}_{200}$ we used as initial conditions the re-analysis $W^{0.1}_{400}$. $W^{0.1}_{400}$ is also used as an initial condition for $E^{0}_{100}/E^{0}_{200}/E^{0}_{400}$ as the re-analysis with $\lambda = 0$ lead to negligible flow variance and cannot be used as warm-up. Our choice for the preferred pair (N_e, λ) is described below (and see Appendix A).

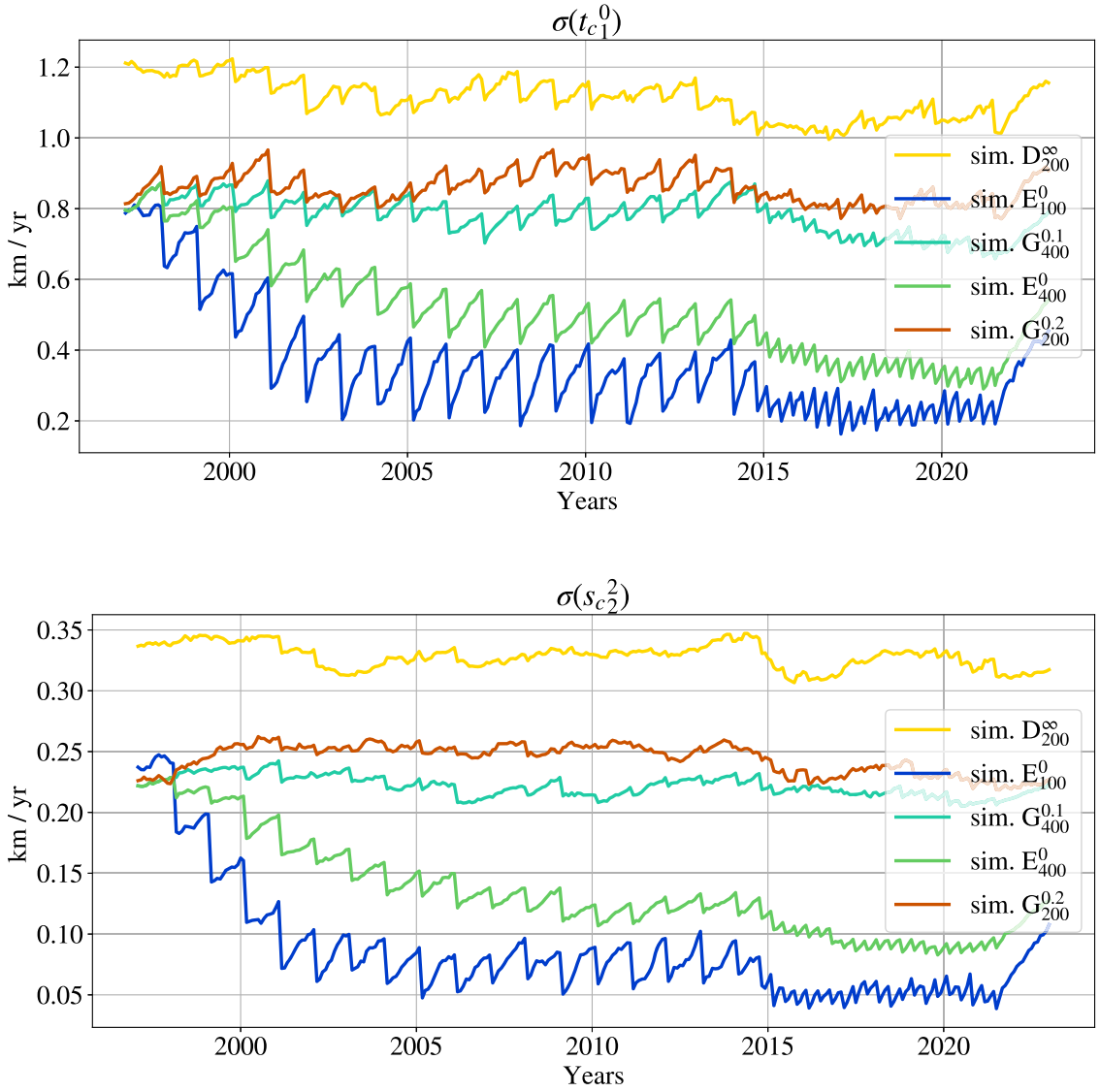

Figure 4. Time evolution of the standard deviation of the flow coefficients $\sigma(t_{c1}^0)$ (top) and $\sigma(s_{c2}^2)$ (bottom) for several reanalysis experiments. Two reanalyses use the empirical estimate $\tilde{P}^f$ of the forecast matrices with $N_e = 100$ (case E_{100}^0) and $N_e = 400$ (case E_{400}^0), and the other two use G-LASSO estimates with $\lambda = 0.1$ and $N_e = 400$ (case $G_{400}^{0.1}$), and with $\lambda = 0.2$ and $N_e = 200$ (case $G_{200}^{0.2}$). See Table 1 for more details.

3.3.4 Ensemble estimates of the forecast covariance matrices

In the original formulation of the ensemble Kalman filter (Evensen 2003), the forecast covariance matrix of a state $\mathbf{x}^f$ is obtained as the sample estimate $\tilde{P}_{xx}^f$ based on a finite number of ensemble realizations. As such it possibly accounts for cross-covariances between elements of the state vector. However, such an estimate can lead to a number of problems related to the finite sample size (Bocquet 2011; Raanes *et al.* 2019), in particular:

(i)an underestimation of the ensemble spread (sometimes leading to an ensemble collapse),
(ii)spurious cross-talking between variables when the covariance matrix, based on a small number of realizations, is too noisy.

As an illustration of the former effect (i), we perform a reanalysis of GVO and GGO observations while considering the crude sample covariance matrices $\tilde{P}_{bb}^f$ and $\tilde{P}_{zz}^f$. We show in Fig. 4 the standard deviation within the ensemble of realizations of the flow coefficients t_{c1}^0 and s_{c2}^2. With $N_e = 100$ (case E_{100}^0), we witness a clear shrinkage of the ensemble spread, with uncertainties decreasing to unrealistic values. This problem barely improves when increasing N_e to 400 (case E_{400}^0), as sampling the forecast error cross-correlations is rather slow, proportional to $1/\sqrt{N_e}$ for a normal sampling. An ensemble of size $N_e \gg N_z$ would be required to obtain in this way a converged estimate of the dense cross-covariance matrix (for example, as performed by Baerenzung *et al.* 2018).

Error (ii) is introduced due to spurious cross-correlations, which are non-zero only due to undersampling. Because the standard deviation on each coefficient of the covariance matrix converges as $1/\sqrt{N_e}$ (Bocquet 2011) the error on weak off-diagonal coefficients can then be of the same order of magnitude as the coefficient itself, resulting in a very poor signal-to-noise ratio, and possibly causing a severe degradation of

the re-analysis performance (Hamill *et al.* 2001). In the worst cases, an incorrect sample covariance matrix may also lead to filter divergence (Bocquet 2011). These issues are well known in oceanography and atmospheric sciences (Ott *et al.* 2004; Berry & Sauer 2013).

Inadequate evaluation of the unknown true covariance matrices in eqs (19) and (22) is a common issue in the EnKF and many avenues have been proposed to tackle the aforementioned problems. Unfortunately, the two main approaches, covariance localization and covariance inflation (e.g. Hamill *et al.* 2001), are not appropriate for our problem. The approach of covariance localization artificially reduces correlations of two points that are well separated in space, an approximation that suits in the atmospheric sciences. However, this approach is difficult to implement when working in the spectral space, because coefficients far apart in the spectral domain can show non-zero correlations – but see the attempt by Sanchez *et al.* (2019), who address this issue by cancelling all correlations between coefficients of different orders m. Furthermore, the physical mechanisms that govern the core surface dynamics operate at planetary scale. Covariance inflation in its most naive form involves artificially increasing the sample covariance matrix at each analysis, for instance replacing $\tilde{P}^f_{xx}$ by $\gamma \tilde{P}^f_{xx}$, with $\gamma > 1$. The parameter γ is picked by trial and error (Anderson & Anderson 1999; Hamill *et al.* 2001), or with an adaptive algorithm to avoid *ad-hoc* tuning (Raanes *et al.* 2019). At first glance, this seems like a relevant solution to deal with the problem of underestimation of the variance. In Hamill *et al.* (2001), the constant inflation factor is set to increase the variance between 0.025 to 4 per cent at each analysis for resp. 400 and 25 realizations; these values are certainly not enough to maintain the variance at a high enough level throughout our reanalysis (see Fig. 4). Another drawback of using covariance inflation for our problem is that a constant γ through time for all coefficients is not appropriate for observations with varying density and quality (Anderson 2009). Although solutions have been proposed to mitigate these issues (Anderson 2009; Bauser *et al.* 2018; Raanes *et al.* 2019), we here consider an alternative solution involving the Graphical lasso technique, which easily adapts to the EnKF formalism.

3.3.5 Handling of the forecast covariance matrix using the graphical lasso algorithm

The dilemma raised in the previous section can be rephrased succinctly: *Given a number of realizations and the associated sampling errors, how many non-zero cross-correlations can we afford to include in our model?* On the one hand, one wishes to keep as many meaningful cross-correlations as possible, in order to reproduce the complex cross-talking between the core flows at large length-scales and subgrid error patterns. On the other hand, the empirical covariance matrix includes spurious correlations that should if possible be removed.

To determine a covariance matrix that conserves as much as possible the information contained into its off-diagonal elements, yet removing many spurious cross-correlations, we use G-LASSO (Friedman *et al.* 2007; Banerjee *et al.* 2008). This algorithm computes the following sparse penalized maximum-likelihood estimator of the precision matrix Θ (inverse of the covariance matrix), by searching for

$$\hat{\Theta}(\lambda) = \mathrm{argmin}_{\Theta \geq 0} \left(\mathrm{tr}(\tilde{P}\Theta) - \log\det(\Theta) + \lambda \sum_{j \neq k} |\Theta_{jk}| \right). \tag{29}$$

$\tilde{P}$ is the sample covariance matrix, input for the algorithm. The first two terms in brackets constitute the log-likelihood of Θ under Gaussian assumptions. The condition $\Theta \geq 0$ imposes that the precision matrix Θ is positive definite. The use of a L_1 norm for the last term in (29) makes $\hat{\Theta}$ sparse. The penalizing parameter λ is a positive real scalar that drives the sparsity of the solution: a large value (in comparison with the off-diagonal elements of $\tilde{P}$) returns a diagonal precision matrix, while a small value for λ results in a solution close to the sample precision matrix, if it exists.

In our case, we are more interested in an estimator of the covariance matrix than the precision matrix. Conveniently, we can choose the inverse of the solution to eq. (29) as an estimator of the covariance matrix (since for reasonable values of λ, such as those favoured in Appendix A, $\hat{\Theta}$ is well conditioned). It happens that $\hat{C} = \hat{\Theta}^{-1}$ is also a sparse matrix. This unintuitive situation where both the estimated covariance and its inverse are sparse is due to the fact that the solution to the dual problem of eq. (29) gives an estimation of the covariance matrix (Banerjee *et al.* 2008), and that the optimal of both the primal and dual problems are equal (Mazumder & Hastie 2012). As G-LASSO performs better when the variance of the different elements in a vector $\mathbf{x}$ have similar scales, we apply here the algorithm to the correlation matrix $\tilde{C}_{xx}$ rather than $\tilde{P}_{xx}$ (with $\mathbf{x}$ standing for either $\mathbf{b}$ or $\mathbf{z}$). Once $\hat{C}_{xx}$ is estimated from $\tilde{C}_{xx}$ using eq. (29), the estimated covariance matrix is computed from the correlation matrix as

$$\hat{P}_{xx}(\lambda) = \mathrm{diag}\left(\tilde{P}_{xx}\right)^{1/2} \hat{C}_{xx}(\lambda) \mathrm{diag}\left(\tilde{P}_{xx}\right)^{1/2}, \tag{30}$$

so that the diagonal of the covariance matrix is kept untouched. In practice we use the scikit-learn implementation of the G-LASSO algorithm (Friedman *et al.* 2007; Pedregosa *et al.* 2011).

$\hat{C}_{zz}$ obtained for different values of λ are presented in Fig. 3. In Appendix A, we show how we choose the penalty parameter λ by solving eq. (29) for several values of λ and maximizing the likelihood. Note that G-LASSO implicitly assumes that our set of realizations follows a Gaussian distribution (not to be confused with LASSO, see Tibshirani 1997). The procedure is applied to obtain both $P^f_{bb}(\lambda)$ and $P^f_{zz}(\lambda)$ before each analysis, and then used in eqs (19) and (22). We readily see from Fig. 4 that no ensemble collapse is observed when using G-LASSO with values of λ in the vicinity of our preferred choice of $\lambda = 0.1$ (resp. 0.2) for $N_e = 400$ (resp. 200). Furthermore, for λ close to this value, a significant part of the anticorrelation expected between $\delta\mathbf{e}^f$ and $\delta\mathbf{f}^f$ is conserved (see Fig. 3). Our new implementation thus constitutes a significant improvement in comparison with that of Gillet *et al.* (2019): in their study although the variance within the ensemble of solutions

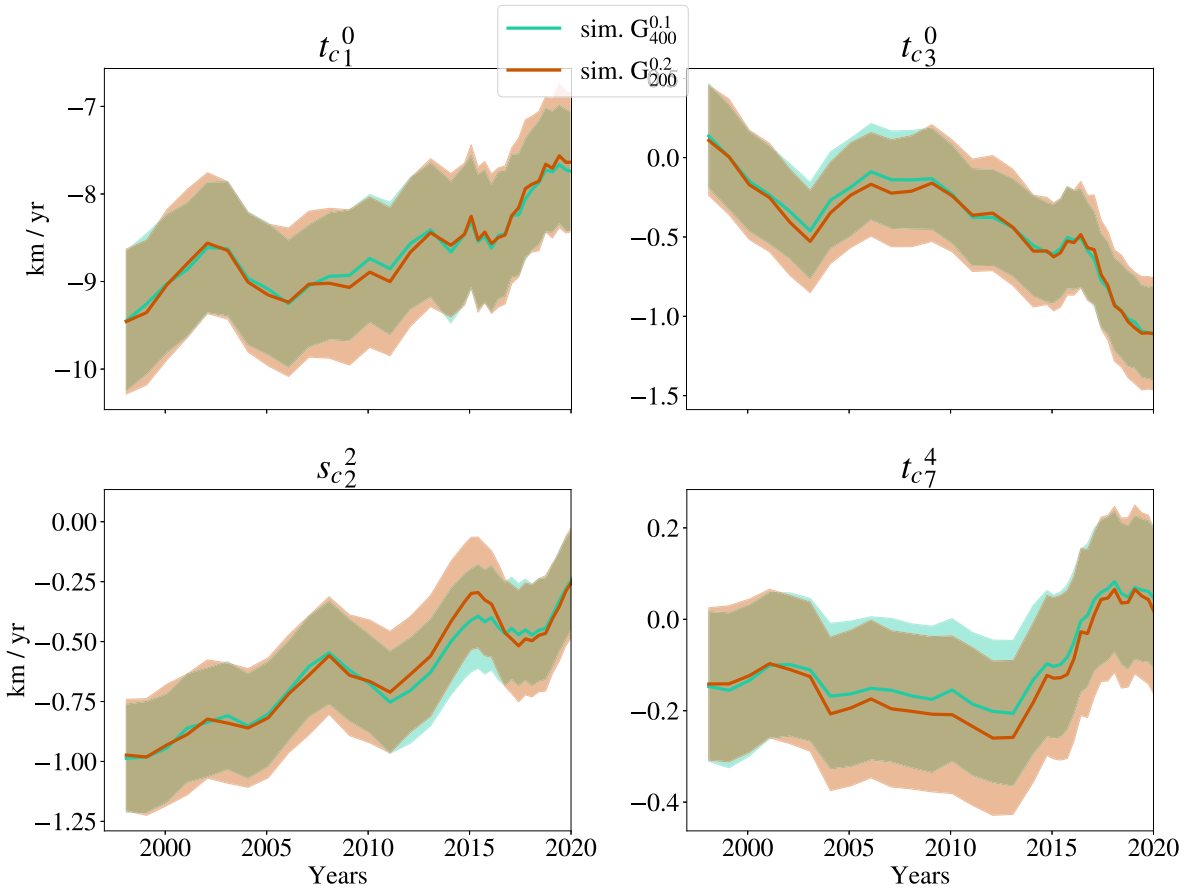

Figure 5. Time-series of some examples of flow coefficients for the two re-analyses $G^{0.2}_{200}$ and $G^{0.1}_{400}$.

for the flow coefficients behaved sensibly, as for the case of a diagonal forecast matrix (see D^{∞}_{200} in Fig. 4), the important cross-covariances mentioned above were clearly ignored.

Finally, we show in Fig. 5 the time evolution of some examples of flow coefficients, together with their associated spread. The two ensemble average flows obtained for reanalyses $G^{0.2}_{200}$ and $G^{0.1}_{400}$ show a very similar time evolution, with differences always much smaller than the associated uncertainties. The dispersion within the ensemble of flows is also very similar for both re-analyses. This indicates that convergence has already been obtained in terms of ensemble size with $N_e = 200$. The use of G-LASSO thus enables stable and converged solutions to be obtained with only limited computing resources, while conserving an important part of the information contained in cross-covariances within the ensemble of realizations, and providing a reasonable measure of the posterior model uncertainties.

3.4 Geomagnetic secular variation over the satellite era

As a result of our reanalysis, a new model of the geomagnetic field evolution is obtained, constrained by both GVO and GGO observations and the dynamics taking place at the surface of Earth's core. In this section we compare this new field model with existing models from the literature, namely the CHAOS-7 model (Finlay *et al.* 2020), and the Kalmag model (Baerenzung *et al.* 2020). The former is a regularized field model smoothed in time by penalizing third time derivatives of the field. The latter is governed in time by stochastic equations embedded into a Kalman filter, and is smoothed *a-posteriori*. Neither of these existing models has constraints on the field time evolution from core surface flow dynamics.

We focus hereafter on the re-analysis $G^{0.1}_{400}$ obtained with $\lambda = 0.1$ and $N_e = 400$ realizations. Fig. 6 illustrates how our model fits SV data at two GGO site examples (Ascension Island and Kourou), and two examples of GVO site (above the Eastern Pacific at low latitude and above Japan at mid-latitude), together with the spread in the ensemble of predictions. It also compares with predictions from the CHAOS-7 and Kalmag models. Beside the local maximum around 2014 on the radial component in Ascension Island (which is not well fit by any of the models), our SV predictions lie within the observation error and fit well the large interannual SV changes responsible of pulses in the secular acceleration (see for instance $\mathrm{d}B_r/\mathrm{dt}$ at Ascension Island and $\mathrm{d}B_\phi/\mathrm{dt}$ in Kourou or above Japan). The amplitude of the analysis prediction spread depends on the amount of data and its quality. It is bigger in the beginning of the reanalysis, when few satellite data are available and observations rely mostly on GGOs (around 1997–2002), gets smaller during the period of best quality CHAMP data (2005–2010). In areas covered by few GGO, it then increases when only CryoSat-2 observations are available (2011–2014), whereas areas well sampled by

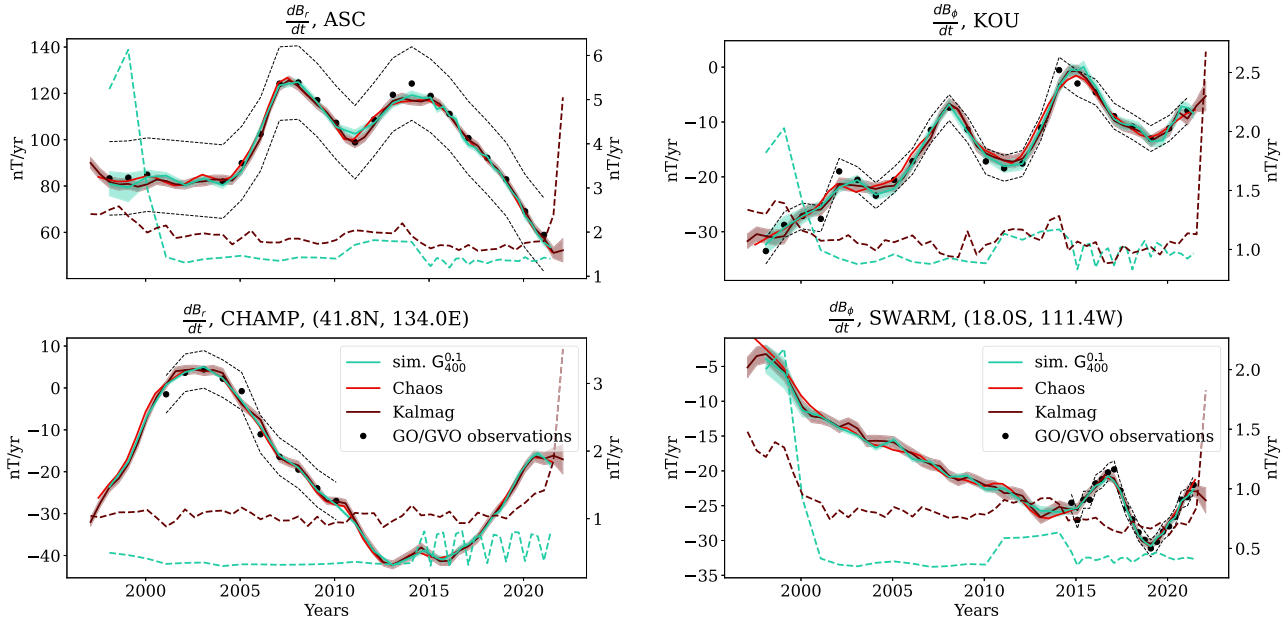

Figure 6. Time-series of SV predictions from the analysed state obtained for $G^{0.1}_{400}$ (cyan), superimposed with those for the CHAOS-7 (red) and Kalmag (brown) models, and compared with observations (black circles). The black thin dashed lines represent the $\pm 1\sigma$ uncertainties on GGO and GVO SV data. Left-hand panel: radial component at the Ascension island GGO (ASC, 7°S, 14°W, sampled every 12 months, top) and at a CHAMP GVO above Japan (41.8N, 134.0E, bottom). Right-hand panel: azimuthal component at the Kourou GGO (KOU, 5°N, 53°W, top), and at a Swarm GVO above the Eastern Pacific at low latitude (18°S, 111°W, sampled every 4 months, bottom). The scale of the SV coefficients is shown on the left-hand side. The standard deviations for the reanalysis $G^{0.1}_{400}$ and for Kalmag are shown in coloured dashed lines, and correspond to the scale on the right and to the thickness of the shaded curve for the model predictions.

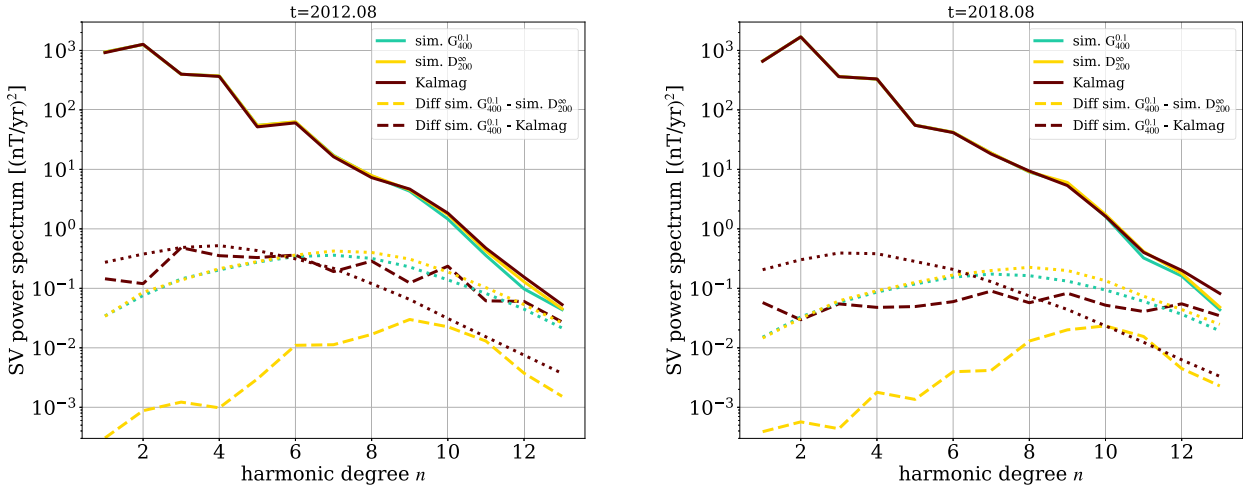

Figure 7. SV Lowes spectra at the Earth's surface for cases $G^{0.1}_{400}$ and D^{∞}_{200}, and compared with the Kalmag model, at epochs 2012.08 (left) and 2018.08 (right): for the ensemble average model (full line), the dispersion within the ensemble of models (dotted lines). Dashed lines represent the spectra for the difference with respect to the model of case $G^{0.1}_{400}$, for the model of case D^{∞}_{200} (yellow) and Kalmag (brown).

GGO show posterior uncertainties less affected by the satellite responsible for the GVO data (see for instance CHAMP above Japan). Finally the spread becomes smallest when Swarm data are available (after 2014). When GVO are available, we obtain uncertainties in general a bit smaller than those provided with Kalmag, though of similar magnitude. In the example of Fig. 6, the spread within the ensemble of analysis predictions in 2020 reaches $\approx$1.6 nT yr^{-1} on dB_r/dt at Ascension Island and 0.4 nT yr^{-1} on dB_ϕ/dt at a Swarm GVO located at 18°S, 111°W (against respectively 1.9 and 0.7 nT yr^{-1} for Kalmag). Uncertainty estimates between the two models are closer in Kourou ($\approx$1 nT yr^{-1}).

We compare in Fig. 7 spatial SV power spectra at the core surface (Lowes 1974),

$$E_{\mathrm{SV}}(n) = (n+1)\sum_{m=0}^{n}(\dot{g}_n^m)^2 + (\dot{h}_n^m)^2\,, \tag{31}$$

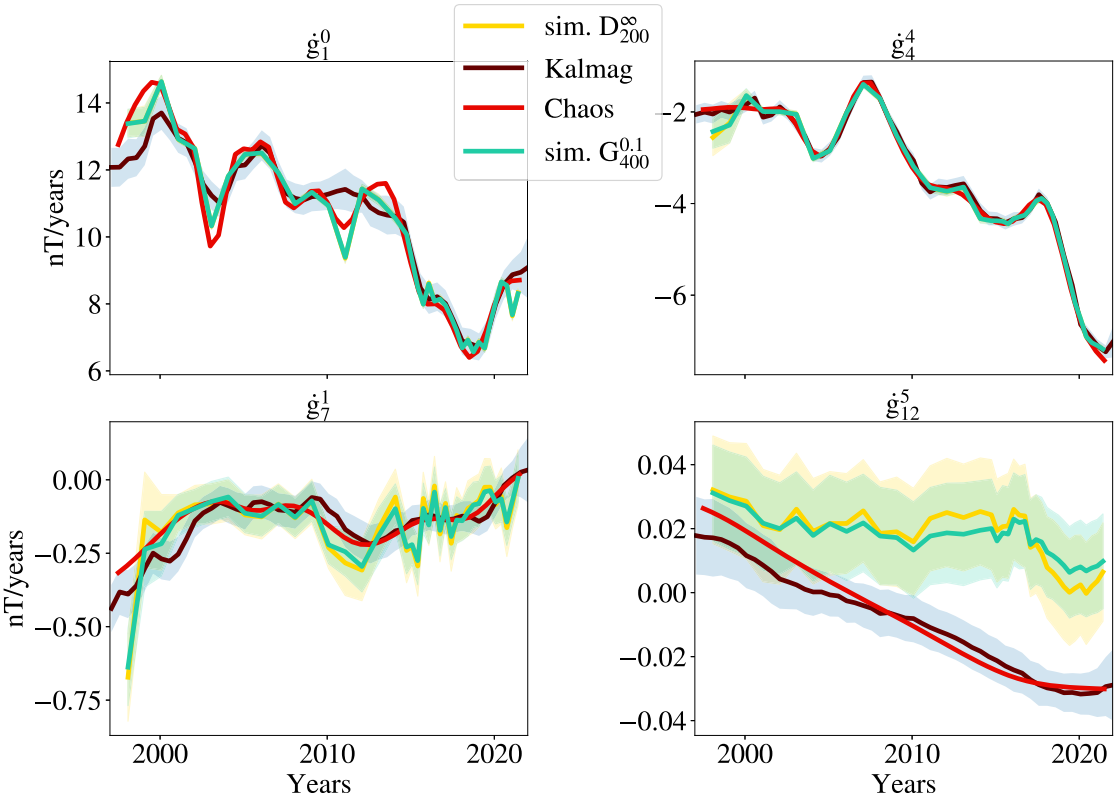

Figure 8. Time-series of the SV Gauss coefficients for cases $G^{0.1}_{400}$ and D^{∞}_{200}, and compared with CHAOS-7 and Kalmag models. The shaded areas represent the $\pm 1\sigma$ standard deviation.

for models of cases $G^{0.1}_{400}$ and D^{∞}_{200}, and Kalmag. At the two epochs considered (2018.08 during Swarm, and 2012.08 when only CryoSat-2 and GGO are available), spectra for the ensemble average solutions almost superimpose, even if we note a slightly larger power for Kalmag at harmonic degrees $n > 10$. Spectra for the dispersion within the ensemble is very similar between the two considered cases ($\lambda = \infty$ and $\lambda = 0.1$). It suggests little effect on the dispersion within the ensemble of SV models when using G-LASSO (compared to a diagonal forecast covariance matrix), likely because the SV is a quantity that is directly observed. Our estimate of posterior SV uncertainties (from the dispersion within the ensemble) is comparable to the difference between our models and Kalmag, for the two epochs considered here. It is larger (resp. smaller) by a factor about 3 than those proposed with Kalmag at small (resp. large) length-scales. The larger uncertainties at large length-scales for Kalmag is coherent with the spread observed for the predicted SV series (see Fig. 6). During the Swarm era, our estimate of these SV errors decreases by a factor $\approx$2 at the largest length-scales (degrees $n \lesssim 6$), in comparison with the period covered by only CryoSat-2 GVO.

Example of SV Gauss coefficient series are shown in Fig. 8. The overall time evolution for our model is comparable to that observed with the other considered field models. This suggests that our assimilation tool is able to build appropriate time-dependent SV estimates. The evolution of near sectorial coefficients agrees particularly closely with other models (see $\dot{g}^4_4$ in Fig. 8), but we witness enhanced high frequency fluctuations in the near zonal coefficients (e.g. $\dot{g}^1_7$), although the other models always lie within $\pm 1\sigma$. Near-zonal coefficients are known to be more difficult to constrain because of possible leakage of external fields near auroral regions (Ropp *et al.* 2020). This is why such coefficients are more heavily damped in CHAOS-7. We recover as in CHAOS-7 some rapid oscillations in $\dot{g}^0_1$ that are absent in Kalmag, for instance around 2011 when Kalmag lacks satellite data, as well as around 2003, when there were gaps in CHAMP data suitable for internal field modelling due to high solar activity. This means there is likely an impact of both the data coverage and the modelling strategy. Note that uncertainties that we provide for the axial dipole are less than those from the Kalmag model. We witness for some high degree coefficients differences between our model and CHAOS-7 or Kalmag that does not fall within the uncertainty level (for instance $\dot{g}^5_{12}$). However, these only represent a tiny contribution to the overall MF model. For all models, caution is needed when interpreting such small length-scale SV structures, for example they are known to be oversmoothed in the CHAOS model. For $\dot{g}^5_{12}$ we estimate uncertainties twice larger than those associated with Kalmag.

4 INFERRED MAGNETOHYDRODYNAMICS OF THE CORE

In this section, we turn to the core surface flow inferred in the reanalysis $G^{0.1}_{400}$, composed of a re-analysis of COV-OBS-x2 Gauss coefficient data from 1880 onwards, and then applied to GGO and GVO when available (see Section 3.3.3). We make use of a cylindrical polar coordinate

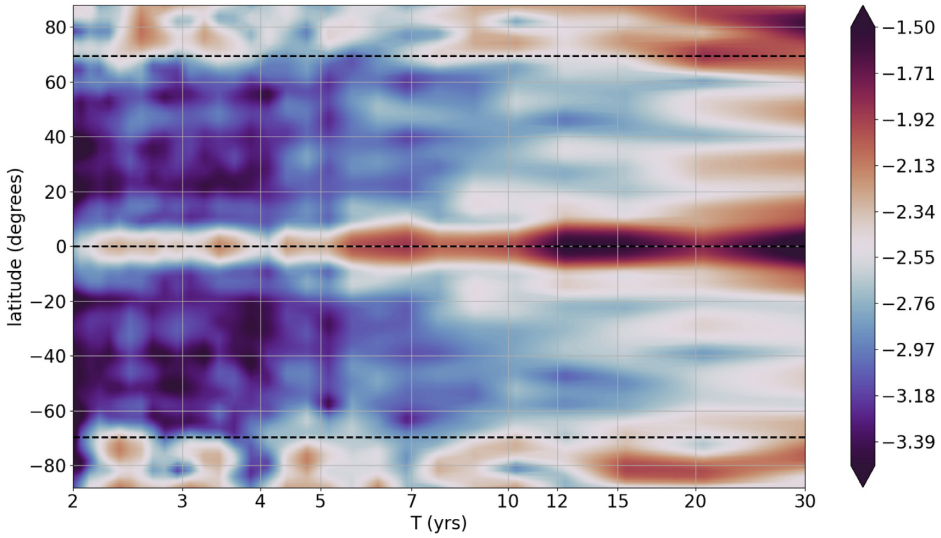

Figure 9. Power in the core surface azimuthal flow acceleration $\partial u_\phi/\partial t$ (in km^2 yr^{-4}) presented on a $\log_{10}$ scale as a function of latitude and period, for the ensemble average solution of our reanalysis $G^{0.1}_{400}$. This spectrogram has been obtained by calculating a power spectrum of the azimuthal flow acceleration series on a $2^\circ \times 2^\circ$ grid at the CMB over the period 1960–2022, after tapering with a Hanning window. The spectra have next been averaged over longitude. Note that 2 yr correspond to the Nyquist period when using a 1 yr sampling rate as used in the input ground GGO and satellite GVO data series (except from Swarm). The black dotted lines indicate the latitudes of the equator and of the intersection between the tangent cylinder and the core surface.

system where unit vectors ($\mathbf{1}_s$, $\mathbf{1}_\phi$, $\mathbf{1}_z$) refer, respectively, to the cylindrical radial, azimuthal and axial (i.e. along the Earth's rotation axis) directions. We present in Fig. 9 a spectrogram for the ensemble average of the azimuthal flow acceleration $\partial u_\phi/\partial t$. It shows enhanced power in the equatorial belt, and to a lesser extent within the tangent cylinder (this hypothetical surface, aligned to $\mathbf{1}_z$ and attached to the inner core, intersects the core surface in two circles of latitudes $\pm 69.5^\circ$). Some period ranges display stronger power. This is the case around 6–7 yr as for the waves documented by Gillet *et al.* (2022), but also at 12–15 yr periods. These bring to mind two broad spectral peaks at interannual and decadal periods, seen in some observatory series towards the equator (see fig. 3 in Lesur *et al.* 2022). These correspond to intense SV changes (some tens of nT yr^{-1}), more clear on the eastward component (the least affected by the magnetospheric ring current), and peak at a period longer than 11 yr the solar cycle period (see also fig. 3 in Lesur *et al.* 2022). This suggests that a significant pollution from external fields on these flow patterns is unlikely. Some power is also present on shorter periods in our flow model with another less intense local maximum around 3.5 yr.

Below we document in more detail these flow patterns. First we investigate in Section 4.1 whether we recover the ∼7 yr wavelike motions similar to Gillet *et al.* (2022) when inverting the dynamics from GGO/GVO data, instead of Gauss coefficients. We also discuss one example of higher frequency motions. Next we consider in Section 4.2 whether similar waves may also exist over longer periods, when considering motions inverted from the COV-OBS-x2 Gauss coefficients. Finally we focus in Section 4.3 on interannual axisymmetric motions, their relation to LOD changes and their interpretation either as torsional Alfvén waves, or as part of the spectrum of QG-MC waves.

4.1 Interannual magneto-Coriolis waves

In Fig. 10, we replicate time-latitude and time-longitude diagrams similar to those presented by Gillet *et al.* (2022), but for our flow models based on Gauss coefficient data from COV-OBS-x2 prior to 1997, and then GVO/GGO data up to 2022. In order to focus on subdecadal motions, where intense SA oscillations have been observed (Chulliat & Maus 2014; Finlay *et al.* 2016), we apply a Butterworth bandpass filter of the order of 2, with a window between 4 and 9.5 yr, to the ensemble average flow model. Over the satellite era, we successfully recover the main patterns interpreted by Gillet *et al.* (2022) as the signature of interannual QG MC waves. The strongest core surface flow features are focused near the equator, where the intensity reaches up to ≈5 km yr^{-1} under the Pacific hemisphere. The flow is primarily equatorially symmetric, as expected for QG motions, and shows evidence of outward propagation at a speed of the order of 150 km yr^{-1} from the tangent cylinder towards the equator. At the equator, we recover a westward propagation of the flow patterns at a speed of the order of ∼1500 km yr^{-1} (Fig. 10, top). There are clearly longitudes of enhanced wave power (e.g. near 180°E or 120°W), indicating the wave patterns can be locally magnified.

Because our flow models have been started based on a longer reanalysis of the COV-OBS-x2 field model, we can also extend backwards in time the analysis of Gillet *et al.* (2022). There are suggestions of similar dynamics (in particular the equatorial focusing) at earlier epochs in the time-latitude diagram near 1970, 1980 and in the 1990's. The first two of these epochs are coincident with well-known jerk events in ground magnetic observatory records (Mandea *et al.* 2010; Lesur *et al.* 2022). They are also periods when some early satellite data (POGO, Magsat and DE-2) is available and contributes to COV-OBS-x2. No clear evidence of the westward propagation is resolved prior to the

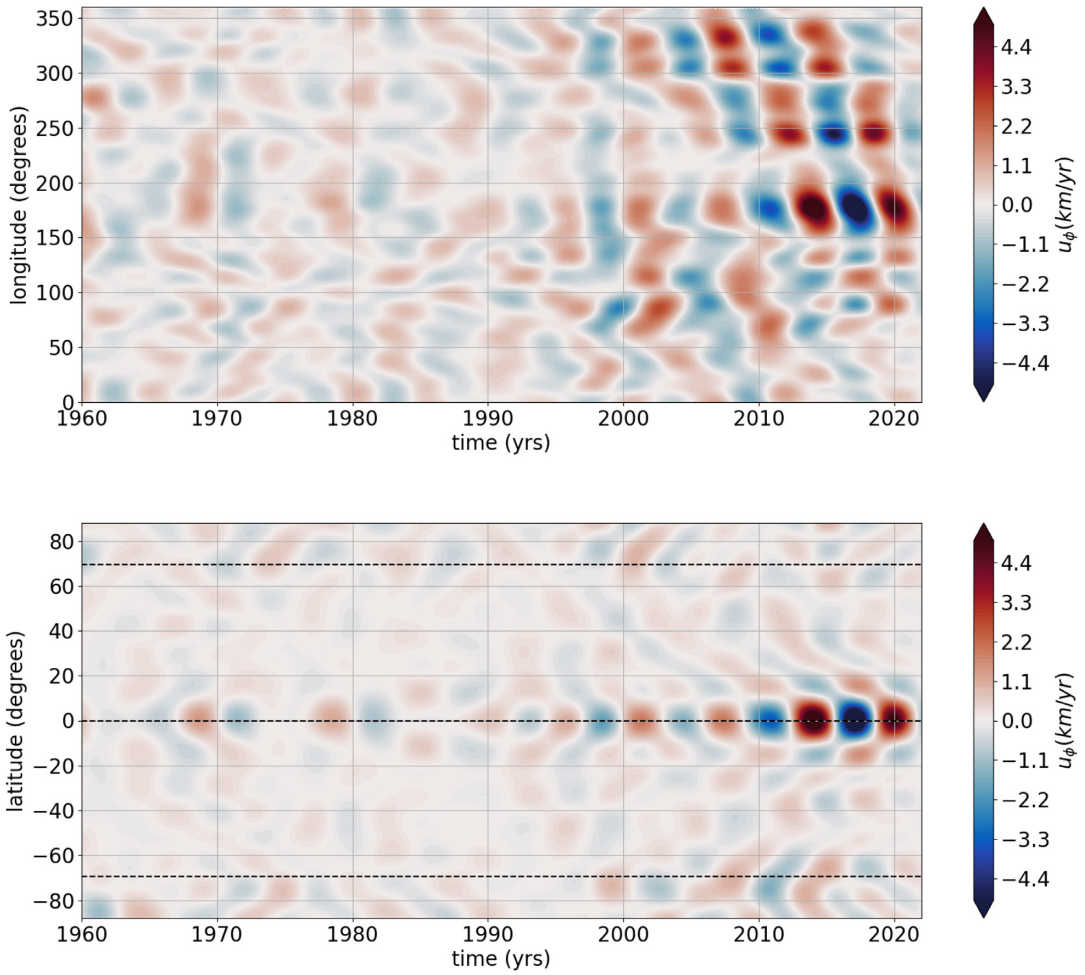

Figure 10. Azimuthal flow (in km yr^{-1}), for the ensemble average solution from reanalysis $G_{400}^{0.1}$, bandpass filtered for $T \in [4, 9.5]$ yr. Time-longitude diagram at the equator (top). Time-latitude diagram at longitude 180°E (bottom), where black dotted lines indicate the latitudes of the equator and of the intersection between the tangent cylinder and the core surface.

satellite era, in agreement with previous results (see fig. 8 in Gillet *et al.* 2019). This possibly results from the limited spatial resolution of non-axisymmetric interannual motions, when the observational constraint comes predominantly from ground-based records.

Motivated by the secondary maximum in the power of the flow acceleration found near the equator at periods around 3.5 yr in Fig. 9, we next investigate higher frequency motions, filtering to retain only periods between 2 and 4 yr. Within this frequency range we again witness a clear outward propagation of wave-like patterns (see the time-latitude diagram for longitude 180°E in Fig. 11, bottom). These transient motions are again mostly equatorially symmetric, and the strongest in the equatorial belt, with a magnitude up to 1.5 km yr^{-1}, so containing significantly less power than the 7 yr waves. They travel at a speed ≈400 km yr^{-1} in the cylindrical radial direction, more than twice faster than the 7 yr waves.

The recovery of these rapid interannual motions is mostly limited to the post-1997 interval of continuous satellite observations in our model; periods shorter than ∼3 yr are filtered by construction in the COV-OBS-x2 model that is used as the data source prior to 1997 (due to spline knot spacing employed in the construction of COV-OBS-x2, see Pick *et al.* 2019). Nevertheless some faint patterns are seen, for instance, during the 1970's. We find no clear evidence for a preferred direction of azimuthal propagation in these patterns at the equator (Fig. 11, top).

4.2 Decadal magneto-Coriolis waves

QG MC waves should also exist on longer timescales where field and flow changes are more intense, since the 7 yr travelling patterns highlighted by Gillet *et al.* (2022) do not constitute the fundamental mode. It is therefore natural to ask whether a detection of such QG MC motions is possible on decadal periods. Motivated by suggestions of a broad spectral peak at some low latitude observatory stations around 15 yr periods (Lesur *et al.* 2022), we bandpass filter our flow solutions for $T \in [10, 20]$ yr. As previously noted by Gillet *et al.* (2015), for such decadal flow changes the largest amplitudes are again seen in the equatorial belt.

We present in Fig. 12 a time-longitude diagram for the azimuthal flow u_ϕ at the equator, and a time-latitude diagram for u_ϕ at 180°E,

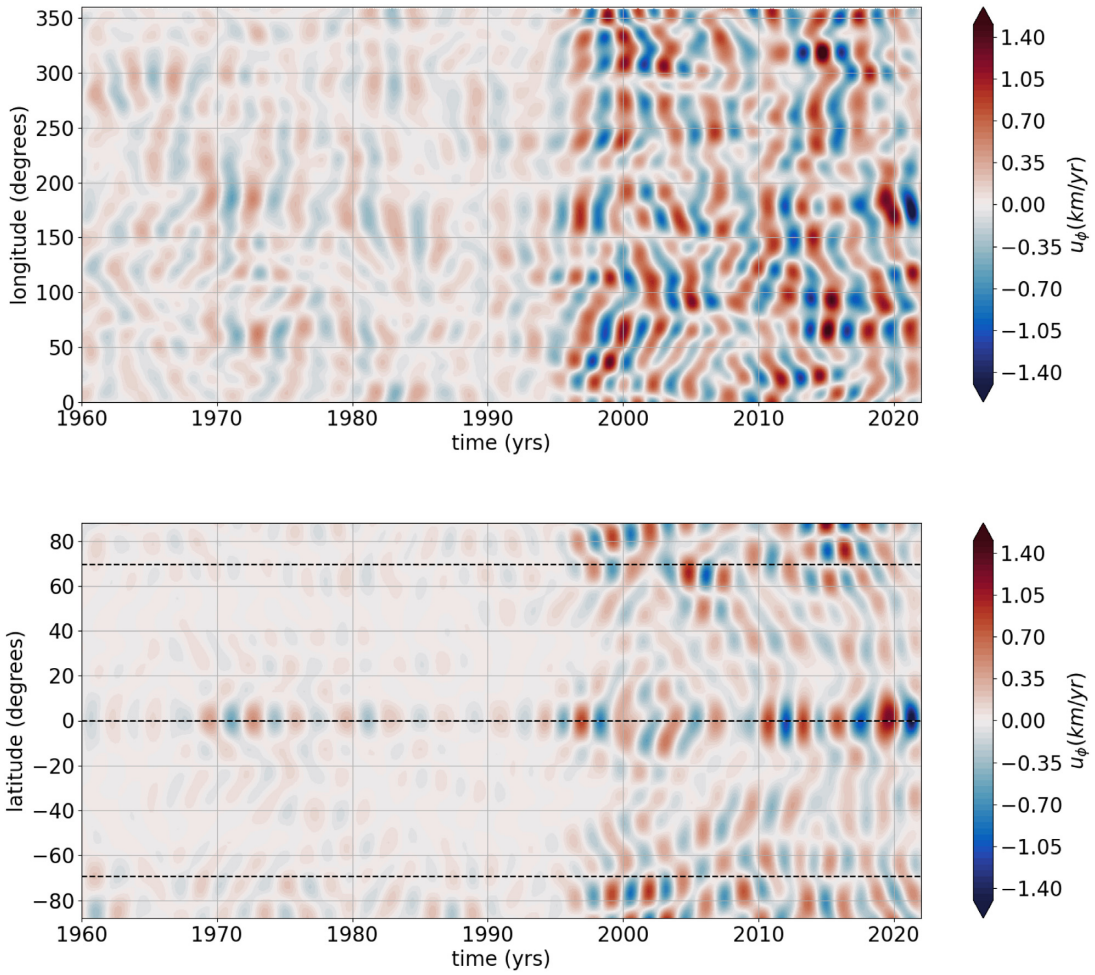

Figure 11. Same as Fig. 10, for the flow band-pass filtered for periods $T \in [2, 4]$ yr.

where these decadal motions are the strongest and reach up to 5 km yr^{-1}. Here again the flow is predominantly equatorially symmetric. Several modulated wave trains appear, typically lasting several decades (i.e. over 2 to 3 periods), with maxima of the envelope centred around 1930 and 1990 (note however there is a damping effect for the most recent epochs associated with filter end-effects). A clear node is observed near $\pm 10^\circ$ in latitudes during those two wave trains, reminiscent of the behaviour for the 7 yr wave documented in Fig. 10. It is replaced by an outward propagation from about 1955 to 1975, at a speed of $\approx$70 km yr^{-1}, less than that found for interannual motions, but still much larger than the convective velocity. Less stringent nodes also appear at higher latitudes.

The similarities between the patterns found on the time-latitude diagrams at interannual and decadal periods suggests the QG MC waves in Earth's core could indeed be present across a broad range of periods. This is in agreement with the behaviour observed in the *71p* geodynamo simulation (Aubert & Gillet 2021), with control parameters approaching Earth's core conditions and which is suitable for studying QG MC waves. In this simulation the presence of numerous spectral lines has been detected in the core surface azimuthal flow, covering a wide range of periods – see fig. 9 of Gillet *et al.* (2022). The strongest signature occurs in the vicinity of the equator, with several nodes present in latitude. Such a dynamo simulation is an arena where both QG Alfvén and QG MC waves are continuously excited (Aubert *et al.* 2022).

Throughout the investigated time-span, the location of the strongest decadal velocity is surprisingly stationary, and centred around 180°E as for the 7 yr waves. For the strongest patterns, some westward drift is seen around 1930 from 60°W to 150°E, while it is mostly stationary in longitude for the second wave train over 1970–2010. QG MC waves potentially propagate both in cylindrical and azimuthal directions. The former is favoured away from the equator, as such waves are elongated along $\mathbf{1}_\phi$, or $k \gg m$ with k and m wavenumbers, respectively, along $\mathbf{1}_s$ and $\mathbf{1}_\phi$. Near the equator, westward drift of wavelike patterns have been documented from both core flow inversions and eigen solutions (Gillet *et al.* 2022). For these latter, the drift appears to be modulated by the local intensity of the cylindrical component of the background field, allowing in principle for complex trajectories in time-longitude diagrams. Furthermore, in the vicinity of the equator, a more accurate derivation of the local dispersion relation is required.

In any case, the consistency of the wave-like patterns documented here across multiple periods nevertheless calls for further investigation. Prior to the satellite era, despite the broad sensitivity of the magnetic data kernels (Gubbins & Roberts 1983), the observational constraints on the time evolution of core surface motions under the equatorial Pacific rely on a limited amount of observatories (in particular from the

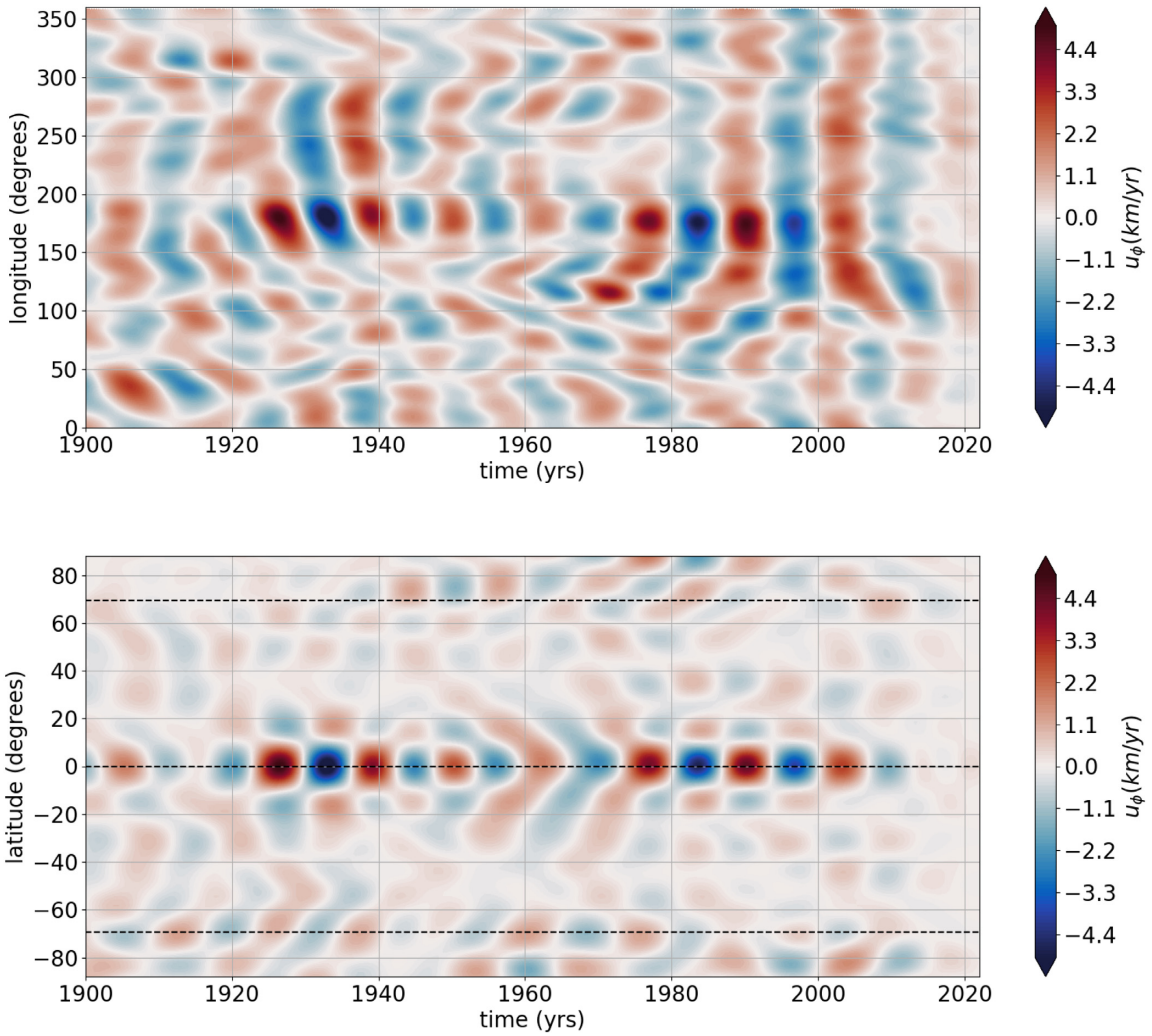

Figure 12. Same as Fig. 10, for the flow band-pass filtered for periods $T \in [10, 20]$ yr.

stations at Honolulu, Apia and Guam). This information is then complemented by the spatiotemporal prior (from the geodynamo simulation), whose importance is not negligible when the observational constraints are more sparse. The recovered flow changes are consistent with the recorded magnetic variations, common to the ensemble of realizations, and can be isolated despite the ensemble spread. Nevertheless, a full evaluation of the quality of the inverted solutions requires dedicated validation experiments based on a synthetic set-up.

4.3 Axisymmetric motions and length-of-day changes

Finally, we turn to transient zonal motions in the core and their relation to changes in the length-of-day. At sub-decadal periods, transient zonal motions inferred from geomagnetic observations have previously been interpreted as torsional Alfvén waves (Gillet *et al.* 2010). Their magnitude is significantly weaker than that of non-zonal flows, by a factor of about 5 (e.g. Gillet *et al.* 2015; Kloss & Finlay 2019). However, because of their simple geometry, it is possible to have a partial access to them even with a less dense networks of observations.

Zonal motions carry angular momentum. In the presence of a coupling with the mantle, it can be transferred to the solid Earth and generate changes in the LOD (e.g. Jault & Finlay 2015). Recent analyses of the LOD series have suggested the existence of distinct sub-decadal spectral lines (e.g. Duan & Huang 2020; Ding *et al.* 2021; Hsu *et al.* 2021), in particular around 6 and 8.5 yr periods. We thus consider the possibility of two different waves, and bandpass filter our ensemble average zonal flow model using a causal Butterworth filters of order 2, with period bands respectively [4.5,7.5] yr and [7.5,9.5] yr (see Fig. 13). The former 6 yr zonal motions show a maximum near the equator that is particularly clear during the satellite era, and less pronounced at earlier epochs. A clear node appears around $\pm 10^\circ$–15° in latitude over the satellite era. Some intense patterns also appear over the past 15 yr within the tangent cylinder in the Southern hemisphere. Conversely, the 8.5 yr zonal motions present a maximum around $\pm 20^\circ$ in latitude, and a local minimum at the equator. They are also associated with intense motions within the tangent cylinder, in both hemispheres. The 8.5 yr pattern appears particularly stable through time (apart from the artificial damping due to the filter near the endpoint, and from the decrease of amplitude in the Southern hemisphere backward in time, that

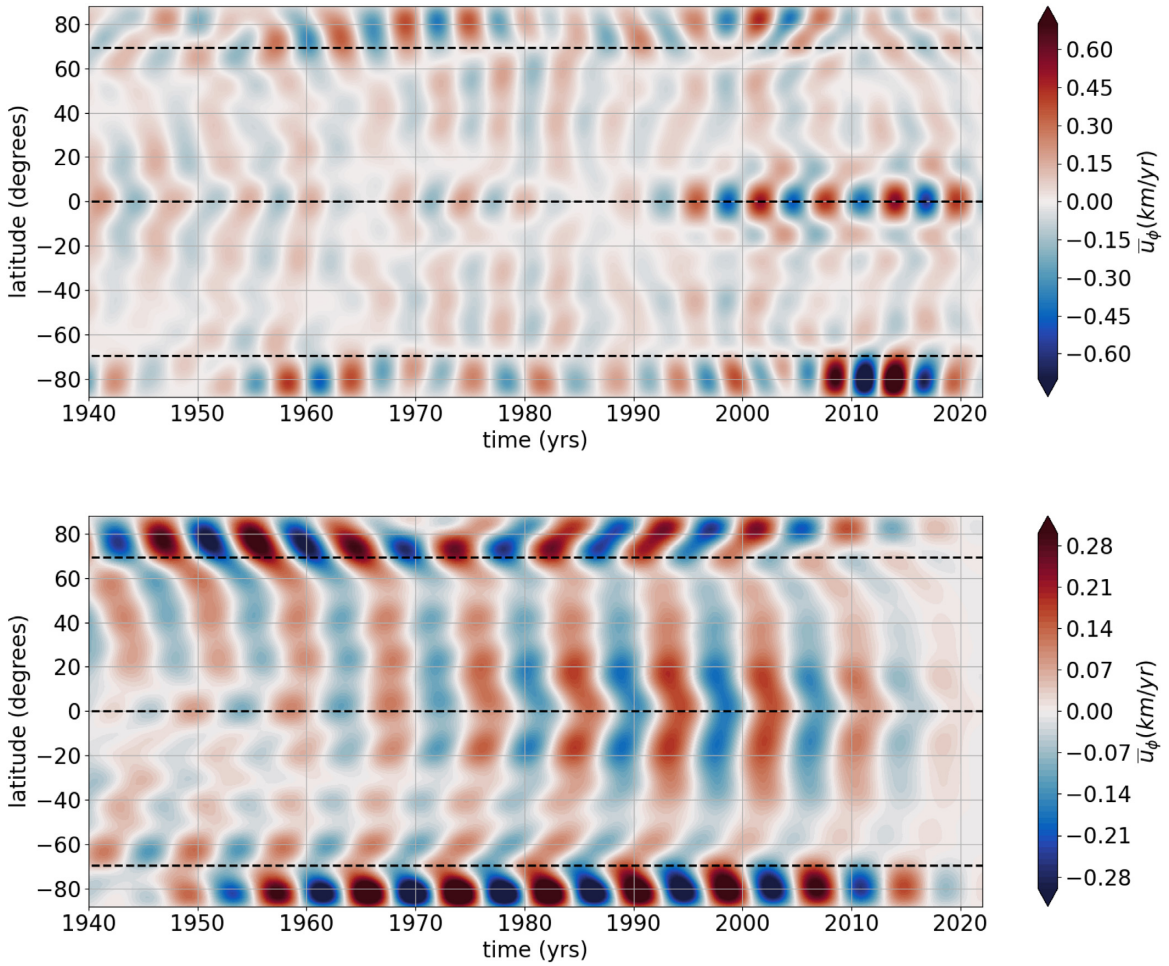

Figure 13. Time-latitude diagram of the axisymmetric azimuthal flow (in km yr^{-1}), bandpass filtered for periods $T \in [4.5, 7.5]$ yr (top), $T \in [7.5, 9.5]$ yr (bottom), for the ensemble average solution from reanalysis $G^{0.1}_{400}$. The black dotted lines indicate the latitudes of the equator and of the intersection between the tangent cylinder and the core surface.

may be data related), with little change after the start of the continuous satellite era. We recover outward propagating patterns similar to those previously identified at earlier epochs, based primarily on the analysis of ground observatory data (Gillet *et al.* 2010).

We compare in Fig. 14 the observed LOD series and the changes in LOD predicted by our flow model. We obtain a convincing fit for the two considered period ranges. It is particularly accurate for the 6 yr signal, though a slight loss of magnitude (for the correct phase) is sometimes observed. The fit to the 8.5 yr signal is particularly good until 1980, while a small phase shift is gradually seen towards the recent epochs, reaching up to $\sim 40^\circ$. When considering both lines together (Fig. 14, bottom), we can conclude that a large part of LOD changes in the period band between 4.5 and 9.5 yr originates from the core.

The rather good fit observed in LOD changes back to the 1940's may appear at odds with (i) the loss of flow magnitude near the equator prior to the satellite era and (ii) the absence of atmospheric correction prior to 1962. Regarding the latter point, although the fit between observed LOD and the core predictions is better after applying the correction, recall that the amplitude of the interannual LOD inferred from our core flow models is larger than that resulting from reanalyses of the atmosphere dynamics at periods around 6 yr (Paek & Huang 2012; Duan *et al.* 2015). Regarding the former point, note that zonal flows near the equator only play a minor role in the angular momentum budget (because geostrophic cylinders there are associated with a tiny moment of inertia). For this reason, the dynamics near the core equator does not significantly impact the LOD signal. The fact the core angular momentum is impacted essentially by large length-scale motions may be part of the reason why it is possible to extract the outer core contribution to LOD change even prior to the era of satellite records.

5 DISCUSSION

5.1 A sparse estimate of the model state cross-covariances

We have above proposed an updated version of the `pygeodyn` data assimilation tool for reconstructing the core surface dynamics from geomagnetic observations. This sequential algorithm is now capable of handling observational information either in the form of Gauss

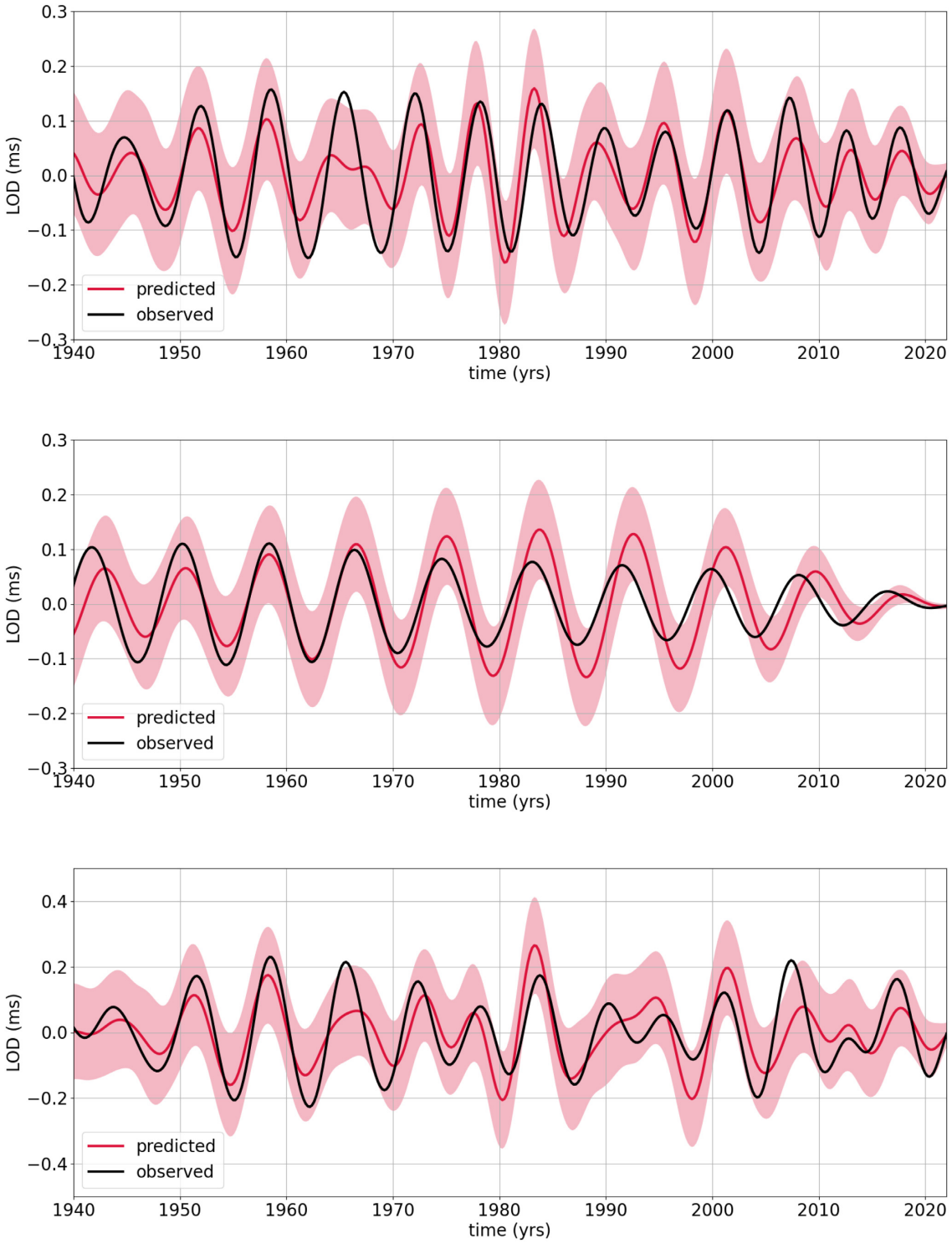

Figure 14. Comparison between the observed and predicted length-of-day changes in the period bands [4.5,7.5] yr (top), [7.5,9.5] yr (middle) and [4.5,9.5] yr (bottom), for the ensemble average solution from reanalysis $G_{400}^{0.1}$. The shaded area represents the $\pm 1\sigma$ standard deviation within the ensemble of solutions.

coefficients, or by means of ground-based and virtual observatory series, whilst at the same time reducing the occurrence of spurious and unphysical time changes.

Our algorithm is furthermore able, through the use of the Graphical lasso method, to account for important cross-covariances within the ensemble of forecast states. The most striking example concerns the anticorrelation between the SV generated by the resolvable flow at large length-scales and that arising from subgrid processes. The origin of such correlations resides in the two contributions to the SV having a common dynamical source, composed of both large and small length-scales, only artificially separated because of the achievable

spatial resolution. Such correlations were so far ignored, despite being important in the effort to extract maximum information from recorded magnetic field changes, especially in a configuration where highly accurate data are explained by the sum of relatively uncertain contributions.

The G-LASSO method for reliably estimating off-diagonal cross-covariance elements allows us to work with ensembles of moderate sizes (thus reducing the computational cost), while producing stable and realistic model state uncertainties. It may also be of interest for alternative assimilation tools based either on reduced stochastic models (Baerenzung *et al.* 2018, 2020) or on geodynamo models (Sanchez *et al.* 2019; Fournier *et al.* 2021).

5.2 QG MC dynamics over a broad range of timescales

The core flow models that we have constructed indicate the presence of QG MC waves across interannual to decadal periods. This description is in agreement with the analysis of recent geodynamo simulations designed to capture rapid core dynamics (Aubert & Gillet 2021; Gillet *et al.* 2022). Our results, via a core flow inversion based directly on ground and virtual observatory data, supports the detection of waves with period ≈7 yr over the past two decades that are well covered by satellite data (Gillet *et al.* 2022). These waves propagate in the cylindrical radial direction at a speed of the order of 150 km yr^{-1}. With a signature at the core surface that is the strongest near the equator, they involve areas of enhanced intensity, in particular under the Pacific around 180°E and 120°W. This observation may be explained in several ways, for example:

(i) Longitudinal changes in the r.m.s. quantity

$$\widetilde{B}_s(s,\phi) = \sqrt{\frac{1}{2H}\int_{-H}^{H} B_s^2(s,\phi,z)\mathrm{d}z} \tag{32}$$

that sustains QG MC waves, with $H = \sqrt{r_C^2 - s^2}$ the half-height of a fluid column,

(ii) Effects of longitudinal variations in the electrical conductance of the deep mantle, to which these waves, like torsional waves (Schaeffer & Jault 2016), are expected to be sensitive,

(iii) The existence of longitudes where buoyant plumes preferentially arise from deep in the core over several decades (Aubert *et al.* 2022).

Although there may be some faint signatures, the detection of the 7 yr QG MC mode at earlier times is not straightforward. This highlights the importance of continuous satellite monitoring of the magnetic field for future recovery of non-zonal interannual core motions.

Peaks in the power of the azimuthal flow acceleration are also observed at both shorter and longer periods, respectively ≈3.5 and 15 yr. In each case the wave-like motions, which are most intense near the equator, are observed to propagate outward. Their meridional speed is respectively faster (≈400 km yr^{-1}) and slower (≈70 km yr^{-1}) for the 3.5 and 15 yr patterns, compared with the 7 yr patterns. We conjecture the existence of QG MC waves over periods ranging from a few years to decades, in agreement with the findings from the *71p* dynamo simulation (Gillet *et al.* 2022; Aubert *et al.* 2022). Although the above relationship between the meridional wave speed and the wave period seems broadly consistent with a local dispersion relation that has been proposed for QG MC waves (Gillet *et al.* 2022), more accurate estimates of the respective wavenumbers and propagation speeds are needed for a proper comparison. Caution is also needed due to (i) sparser spatial coverage at older epochs which affects the decadal estimates and (ii) the difficulty in isolating the core signal on periods as short as a couple of years, in particular towards high latitudes (Baerenzung *et al.* 2020; Finlay *et al.* 2020; Ropp *et al.* 2020). Dedicated synthetic validation studies are needed to help assess the impact on the recovery of the strength of the wave forcing, the data coverage and the considered timescale.

Towards periods shorter than ≈2 yr, numerical simulations suggest the presence of QG Alfvén (instead of QG MC) waves, where the balance is between Lorentz forces and inertia, with little impact of the Coriolis force (Aubert & Finlay 2019; Aubert & Gillet 2021). Their occurrence is thought to be more likely towards mid-latitudes, as they tend to morph into QG MC waves when propagating outward towards the equator where the QG columns are shorter (Aubert *et al.* 2022). QG Alfvén waves are also expected to involve smaller length-scales than QG MC waves, for a given column height and field strength (Gillet *et al.* 2022). They therefore seem difficult to target with the resolution currently available from observations.

Moving to periods similar to or longer than the turn-over time (say 100 yr), the background field has enough time to significantly evolve. This could hinder the propagation of QG MC waves. Furthermore, when considering increasing periods, the propagation speed of QG MC waves will at some stage reach the convection speed, so that isolating them by filtering methods becomes more difficult. In such a case a description of QG MC waves based on a limited set of linear eigenmodes may not be relevant, and they may significantly interact with the background state due to their increasing magnetic energy towards low frequencies. Nevertheless, the fact that clear spectral lines are found at centennial periods in spectrograms of the surface velocity for the *71p* model (Gillet *et al.* 2022) suggests there may be no fundamental barrier to QG MC waves existing on longer periods. A possible explanation may reside in the r.m.s. quantity $\widetilde{B}_s(s,\phi)$ being relatively stable over several centuries, despite the significant evolution of the dynamo field over such timescales.

5.3 Several sources to geostrophic motions and the LOD

Various possibilities can be envisioned regarding the origin of interannual geostrophic motions, and associated changes in the LOD. An obvious solution is in terms of torsional waves (Braginsky 1970), which are axisymmetric solutions to the dynamics in a sphere (or a spherical

shell) in the presence of rotation and a background magnetic field with a non-zero component along $\mathbf{1}_s$. Because of the boundary conditions, the period of torsional mode harmonics is not necessarily an integer fraction of the fundamental mode (Gillet *et al.* 2017). It is thus possible to have two distinct torsional modes at 6 and 8.5 yr periods. Transferring the fundamental mode from 6 yr, as proposed by Gillet *et al.* (2010), to 8.5 yr will have little affect on their estimate of the field intensity deep in the core, because this latter quantity was estimated from the slowness (time required to cross the outer core) and not the period–despite the slowness and the period being related, a difference between the two can be accommodated by the effect of boundaries. Nevertheless, in such a scenario, it remains to be explained why the 8.5 yr mode would not show a maximum at the equator, as seen in all the eigenmodes calculated by Gillet *et al.* (2017). Perhaps this observation might provide some information concerning the boundary conditions.

Meanwhile, a second possible solution is associated with QG MC waves. These were excluded up to now because they were thought to be irrelevant on interannual periods, as far as the observable part of the magnetic signal is concerned. Their discovery from magnetic data at a period close to 7 yr (Gerick *et al.* 2021; Gillet *et al.* 2022) provides a new family of candidates for interannual zonal motions. In a case where the background field is non-axisymmetric, as it is the case in Earth's core, QG MC modes project onto several azimuthal waves numbers, and thus possibly contain an axisymmetric contribution, anchored to non-zonal motions (Labbé *et al.* 2015). This property follows directly from the differential equation set-up by Taylor (1963) for magnetostrophic dynamics (i.e. where inertia can be neglected, and time changes are governed by the induction equation). On interannual timescales, the magnetostrophic branch of the QG MC modes considered by Taylor (1963) approaches the torsional Alfvén branch if one reinstates the role of inertia and considers a field with a non-zero $\widetilde{B}_s$, as has been done by Gerick *et al.* (2021).

In both cases (torsional or QG MC waves), what sustains the waves is the cylindrical radial component of the background field (see the dispersion relation in Gillet *et al.* 2022). Investigation of the second possibility for explaining variations in the LOD requires calculations of QG MC waves in the presence of a coupling with the mantle. The existence of QG MC waves on decadal and longer periods (where inertia is of secondary importance) may also explain the LOD changes observed on these timescales.

5.4 Predicting geomagnetic field changes

One may question the ability of models (reduced or not) to predict geomagnetic field changes. If the physics governing interannual to decadal changes is based on QG MC waves, predicting the SV involves an accurate description of the associated modes, whether it be through a deterministic or a stochastic representation. A deterministic description requires knowledge of the background field $\tilde{B}_s(s,\phi)$, and further research is needed to characterize the sensitivity of the QG MC waves to this quantity.

By construction, numerical dynamo models following the path described by Aubert *et al.* (2017) are largely unchanged regarding their characteristics on long timescales as one moved towards Earth-like conditions. The magnetic diffusion time $\tau_\eta = r_C^2/\eta \sim 130$ kyr, the turn-over time $\tau_u \sim 130$ yr (and consequently the magnetic Reynolds number $R_m = Ur_C/\eta = \tau_\eta/\tau_U \sim 10^3$), and also the Elsasser number $\Lambda = B^2/(2\rho\mu\eta\Omega) \sim 1$, ratio of magnetic to rotation forces on long timescales, are all unchanged moving along the path. The Elsasser number can be rewritten as $\Lambda = \tau_\eta\tau_\Omega/\tau_A^2$ (with $\tau_\Omega = 1/\Omega$ the rotation timescale), so it turns out the timescale associated with MC waves $\tau_{MC} \propto \tau_A^2/\tau_\Omega$ is also invariant along the path (for given wavenumbers in the s and ϕ directions). The important point here is that as one progresses along the path, the range of timescales that can be considered as Earth-like extends towards short periods, so that a wider range of QG MC modes harmonics can possibly be captured in the numerical model.

For reduced stochastic models as that considered here, the ability to mimic geomagnetic field changes should thus extend towards shorter periods as they are derived from dynamos lying further and further along the path. At periods shorter than $\approx\tau_A$, for which the dynamo is not geophysically realistic and that should not be considered for building the reduced equations, the stochastic forcing will in all cases dominate. The relevance of SV prediction from stochastic models will therefore again depend on the sensitivity of the QG MC waves to the background $\tilde{B}_s$. The above stochastic model has been derived by stacking over snapshots covering a long time span ($\approx$10 kyr), assuming stationary statistics. A high sensitivity to the slowly evolving background field might then reduce its predictive power. Non-Gaussian characteristics of the dynamo statistics, that violate the assumptions of the linear stochastic model considered here, may also impact its predictive ability. Further work is needed in the future to better characterize the predictive ability of reduced stochastic models such as that studied here.

AVAILABILITY OF DATA SETS AND MATERIAL

The GGO and GVO data sets are available from https://doi.org/10.11583/DTU.19306886.v1. The python code for calculating core flows, as well as the magnetic and flow models proposed in this study will be made available from https://geodyn.univ-grenoble-alpes.fr/.

ACKNOWLEDGMENTS

We thank the two anonymous reviewers, whose comments helped improve the quality of the manuscript. We wish to thank ESA for the prompt availability of *Swarm* L1b data and for providing access to the CryoSat-2 platform magnetometer data and related engineering information. The support of the CHAMP mission by the German Aerospace Center (DLR) and the Federal Ministry of Education and Research for the

CHAMP mission is gratefully acknowledged. The Ørsted Project was made possible by extensive support from the Danish Government, NASA, ESA, CNES, DARA and the Thomas B. Thriges Foundation. The staff of the geomagnetic observatories and INTERMAGNET are thanked for supplying high-quality observatory data. This work has been funded by ESA in the framework of EO Science for Society, through contract 4000127193/19/NL/IA (Swarm+4D Deep Earth: Core). It was also partially supported by the CNES. NG and MI are part of Labex OSUG@2020 (ANR10 LABX56).

REFERENCES

Anderson, J., 2009. Spatially and temporally varying adaptive covariance inflation for ensemble filters, *Tellus A,* **61**(1), 72–83.

Anderson, J.L. & Anderson, S.L., 1999. A Monte Carlo implementation of the nonlinear filtering problem to produce ensemble assimilations and forecasts, *Mon. Weather Rev.,* **127**(12), 2741–2758.

Aubert, J., 2015. Geomagnetic forecasts driven by thermal wind dynamics in the Earth's core, *Geophys. J. Int.,* **203**(3), 1738–1751.

Aubert, J., 2018. Geomagnetic acceleration and rapid hydromagnetic wave dynamics in advanced numerical simulations of the geodynamo, *Geophys. J. Int.,* **214**(1), 531–547.

Aubert, J., 2020. Recent geomagnetic variations and the force balance in Earth's core, *Geophys. J. Int.,* **221**(1), 378–393.

Aubert, J. & Finlay, C.C., 2019. Geomagnetic jerks and rapid hydromagnetic waves focusing at Earth's core surface, *Nat. Geosci.,* **12**(5), 393–398.

Aubert, J. & Gillet, N., 2021. The interplay of fast waves and slow convection in geodynamo simulations nearing Earth's core conditions, *Geophys. J. Int.,* **225**(3), 1854–1873.

Aubert, J., Gastine, T. & Fournier, A., 2017. Spherical convective dynamos in the rapidly rotating asymptotic regime, *J. Fluid Mech.,* **813,** 558–593.

Aubert, J., Livermore, P.W., Finlay, C.C., Fournier, A. & Gillet, N., 2022. A taxonomy of simulated geomagnetic jerks, *Geophys. J. Int.,* **231,** 650–672.

Baerenzung, J., Holschneider, M., Wicht, J., Sanchez, S. & Lesur, V., 2018. Modeling and predicting the short-term evolution of the geomagnetic field, *J. geophys. Res.: Solid Earth,* **123**(6), 4539–4560.

Baerenzung, J., Holschneider, M., Wicht, J., Lesur, V. & Sanchez, S., 2020. The Kalmag model as a candidate for IGRF-13, *Earth Planets Space,* **72**(1), 1–13.

Banerjee, O., El Ghaoui, L. & d'Aspremont, A., 2008. Model selection through sparse maximum likelihood estimation for multivariate Gaussian or binary data, *J. Mach. Learn. Res.,* **9,** 485–516.

Barrois, O., Hammer, M.D., Finlay, C.C., Martin, Y. & Gillet, N., 2018. Assimilation of ground and satellite magnetic measurements: inference of core surface magnetic and velocity field changes, *Geophys. J. Int.,* **215,** 695–712.

Bauser, H.H., Berg, D., Klein, O. & Roth, K., 2018. Inflation method for ensemble kalman filter in soil hydrology, *Hydrol. Earth Syst. Sci.,* **22**(9), 4921–4934.

Beggan, C.D. & Whaler, K.A., 2018. Ensemble kalman filter analysis of magnetic field models during the champ-swarm gap, *Phys. Earth planet. Inter.,* **281,** 103–110.

Beggan, C.D., Whaler, K.A. & Macmillan, S., 2009. Biased residuals of core flow models from satellite-derived virtual observatories, *Geophys. J. Int.,* **177**(2), 463–475.

Berry, T. & Sauer, T., 2013. Adaptive ensemble Kalman filtering of nonlinear systems, *Tellus A,* **65**(1), 20331.

Bizouard, C. & Gambis, D., 2009. The combined solution c04 for Earth orientation parameters consistent with international terrestrial reference frame 2005, in *Geodetic Reference Frames,* pp. 265–270, ed. Drewes, H., Springer.

Bocquet, M., 2011. Ensemble Kalman filtering without the intrinsic need for inflation, *Nonlinear Process. Geophys.,* **18**(5), 735–750.

Braginsky, S.I., 1970. Torsional magnetohydrodynamic vibrations in the Earth's core and variations in day length, *Geomag. Aeron.,* **10,** 1–8.

Canet, E., Finlay, C.C. & Fournier, A., 2014. Hydromagnetic quasi-geostrophic modes in rapidly rotating planetary cores, *Phys. Earth planet. Inter.,* **229,** 1–15.

Chulliat, A. & Maus, S., 2014. Geomagnetic secular acceleration, jerks, and a localized standing wave at the core surface from 2000 to 2010, *J. geophys. Res.: Solid Earth,* **119**(3), 1531–1543.

Ding, H., An, Y. & Shen, W., 2021. New evidence for the fluctuation characteristics of intradecadal periodic signals in length-of-day variation, *J. geophys. Res.: Solid Earth,* **126**(2), e2020JB020990.

Dobslaw, H., Dill, R., Grötzsch, A., Brzeziński, A. & Thomas, M., 2010. Seasonal polar motion excitation from numerical models of atmosphere, ocean, and continental hydrosphere, *J. geophys. Res.: Solid Earth,* **115**(B10).

Duan, P. & Huang, C., 2020. Intradecadal variations in length of day and their correspondence with geomagnetic jerks, *Nat. Commun.,* **11**(1), 1–8.

Duan, P., Liu, G., Liu, L., Hu, X., Hao, X., Huang, Y., Zhang, Z. & Wang, B., 2015. Recovery of the 6-year signal in length of day and its long-term decreasing trend, *Earth Planets Space,* **67**(1), 1–11.

Evensen, G., 2003. The ensemble Kalman filter: theoretical formulation and practical implementation, *Ocean Dyn.,* **53**(4), 343–367.

Farquharson, C.G. & Oldenburg, D.W., 1998. Non-linear inversion using general measures of data misfit and model structure, *Geophys. J. Int.,* **134**(1), 213–227.

Finlay, C., Lesur, V., Thébault, E., Vervelidou, F., Morschhauser, A. & Shore, R., 2017. Challenges handling magnetospheric and ionospheric signals in internal geomagnetic field modelling, *Space Sci. Rev.,* **206**(1), 157–189.

Finlay, C., Kloss, C., Olsen, N., Hammer, M., Tøffner-Clausen, L., Grayver, A. & Kuvshinov, A., 2020. The CHAOS-7 geomagnetic field model and observed changes in the South Atlantic Anomaly, *Earth Planets Space,* **72**(1), 1–31.

Finlay, C.C., Olsen, N., Kotsiaros, S., Gillet, N. & Tøffner-Clausen, L., 2016. Recent geomagnetic secular variation from swarm and ground observatories as estimated in the CHAOS-6 geomagnetic field model, *Earth Planets Space,* **68**(1), 1–18.

Fournier, A. *et al.*, 2010. An introduction to data assimilation and predictability in geomagnetism, *Space Sci. Rev,* **155**(1–4), 247–291.

Fournier, A., Aubert, J. & Thébault, E., 2015. A candidate secular variation model for IGRF-12 based on Swarm data and inverse geodynamo modelling, *Earth Planets Space,* **67**(1), 1–17.

Fournier, A., Aubert, J., Lesur, V. & Thébault, E., 2021. Physics-based secular variation candidate models for the IGRF, *Earth Planets Space,* **73**(1), 1–18.

Friedman, J., Hastie, T. & Tibshirani, R., 2007. Sparse inverse covariance estimation with the graphical lasso, *Biostatistics,* **9**(3), 432–441.

Gerick, F., Jault, D. & Noir, J., 2021. Fast quasi-geostrophic magneto-Coriolis modes in the Earth's core, *Geophys. Res. Lett.,* **48**(4), e2020GL090803.

Gillet, N., 2019. Spatial and temporal changes of the geomagnetic field: insights from forward and inverse core field models, in *Geomagnetism, Aeronomy and Space Weather: a Journey from the Earth's Core to the Sun,* pp. 115–132, eds Mandea, M., Korte, M., Yau, A. & Petrovsky, E., Cambridge Univ. Press.

Gillet, N., Jault, D., Canet, E. & Fournier, A., 2010. Fast torsional waves and strong magnetic field within the Earth's core, *Nature,* **465**(7294), 74–77.

Gillet, N., Jault, D., Finlay, C. & Olsen, N., 2013. Stochastic modeling of the Earth's magnetic field: inversion for covariances over the observatory era, *Geochem. Geophys. Geosyst.,* **14**(4), 766–786.

Gillet, N., Jault, D. & Finlay, C.C., 2015. Planetary gyre, time-dependent eddies, torsional waves, and equatorial jets at the Earth's core surface, *J. geophys. Res.: Solid Earth,* **120**(6), 3991–4013.

Gillet, N., Jault, D. & Canet, E., 2017. Excitation of travelling torsional normal modes in an Earth's core model, *Geophys. J. Int.,* **210**(3), 1503–1516.

Gillet, N., Huder, L. & Aubert, J., 2019. A reduced stochastic model of core surface dynamics based on geodynamo simulations, *Geophys. J. Int.,* **219**(1), 522–539.

Gillet, N., Gerick, F., Angappan, R. *et al.*, 2022. A dynamical prospective on interannual geomagnetic field changes, *Surv. Geophys.,* **43,** 71–105.

Gillet, N., Gerick, F., Jault, D., Schwaiger, T., Aubert, J. & Istas, M., 2022. Satellite magnetic data reveal interannual waves in Earth's core, *Proc. Natl. Acad. Sci. U.S.A.,* **119**(13), e2115258119.

Gross, R.S., 2001. A combined length-of-day series spanning 1832–1997: Lunar97, *Phys. Earth planet. Inter.,* **123**(1), 65–76.

Gubbins, D. & Roberts, N., 1983. Use of the frozen flux approximation in the interpretation of archaeomagnetic and palaeomagnetic data, *Geophys. J. Int.,* **73**(3), 675–687.

Hamill, T.M., Whitaker, J.S. & Snyder, C., 2001. Distance-dependent filtering of background error covariance estimates in an ensemble kalman filter, *Mon. Weather Rev.,* **129**(11), 2776–2790.

Hammer, M.D., Cox, G.A., Brown, W.J., Beggan, C.D. & Finlay, C.C., 2021a. Geomagnetic virtual observatories: monitoring geomagnetic secular variation with the swarm satellites, *Earth Planets Space,* **73**(1), 1–22.

Hammer, M.D., Finlay, C.C. & Olsen, N., 2021b. Applications for cryosat-2 satellite magnetic data in studies of Earth's core field variations, *Earth Planets Space,* **73**(1), 1–22.

Hide, R., 1966. Free hydromagnetic oscillations of the Earth's core and the theory of the geomagnetic secular variation, *Philos. Trans. Royal Soc. A,* **259**(1107), 615–647.

Holme, R., 2015. Large scale flow in the core, in *Treatise in Geophysics, Core Dynamics, Vol. 8, chap. 4,* pp. 91–113, eds Olson, P. & Schubert, G., Elsevier.

Holme, R. & De Viron, O., 2013. Characterization and implications of intradecadal variations in length of day, *Nature,* **499**(7457), 202–204.

Hori, K., Teed, R. & Jones, C., 2018. The dynamics of magnetic Rossby waves in spherical dynamo simulations: a signature of strong-field dynamos?, *Phys. Earth planet. Inter.,* **276,** 68–85.

Hsu, C.-C., Duan, P.-S., Xu, X.-Q., Zhou, Y.-H. & Huang, C.-L., 2021. On the ~ 7 year periodic signal in length of day from a frequency domain stepwise regression method, *J. Geod.,* **95**(5), 1–15.

Huder, L., Gillet, N. & Thollard, F., 2019. pygeodyn 1.1. 0: a python package for geomagnetic data assimilation, *Geosci. Model Dev.,* **12**(8), 3795–3803.

Huder, L., Gillet, N., Finlay, C.C., Hammer, M.D. & Tchoungui, H., 2020. COV-OBS. x2: 180 years of geomagnetic field evolution from ground-based and satellite observations, *Earth Planets Space,* **72**(1), 1–18.

Jault, D. & Finlay, C., 2015. Waves in the core and mechanical core–mantle interactions, in *Treatise on Geophysics: Core Dynamics,* pp. 225–245, ed. Schubert, G., Elsevier.

Kloss, C. & Finlay, C.C., 2019. Time-dependent low-latitude core flow and geomagnetic field acceleration pulses, *Geophys. J. Int.,* **217**(1), 140–168.

Labbé, F., Jault, D. & Gillet, N., 2015. On magnetostrophic inertia-less waves in quasi-geostrophic models of planetary cores, *Geophys. Astrophys. Fluid Dyn.,* **109**(6), 587–610.

Leopardi, P., 2006. A partition of the unit sphere into regions of equal area and small diameter, *Electron. Trans. Numer,* **25**(12), 309–327.

Lesur, V., Gillet, N., Hammer, M.D. *et al.*, 2022. Rapid variations of Earth's core magnetic field, *Surv. Geophys.,* **43,** 41–69.

Lowes, F., 1974. Spatial power spectrum of the main geomagnetic field, and extrapolation to the core, *Geophys. J. Int.,* **36**(3), 717–730.

Macmillan, S. & Olsen, N., 2013. Observatory data and the Swarm mission, *Earth Planets Space,* **65,** 1355–1362.

Mandea, M. & Olsen, N., 2006. A new approach to directly determine the secular variation from magnetic satellite observations, *Geophys. Res. Lett.,* **33**(15).

Mandea, M., Holme, R., Pais, A., Pinheiro, K., Jackson, A. & Verbanac, G., 2010. Geomagnetic jerks: rapid core field variations and core dynamics, *Space Sci. Rev,* **155**(1), 147–175.

Mazumder, R. & Hastie, T., 2012. The graphical lasso: new insights and alternatives, *Electron. J. Stat.,* **6,** 2125–2149.

Olsen, N., 2002. A model of the geomagnetic field and its secular variation for epoch 2000 estimated from ørsted data, *Geophys. J. Int.,* **149**(2), 454–462.

Olsen, N. & Mandea, M., 2007. Investigation of a secular variation impulse using satellite data: the 2003 geomagnetic jerk, *Earth planet. Sci. Lett.,* **255**(1), 94–105.

Olsen, N., Lühr, H., Finlay, C.C., Sabaka, T.J., Michaelis, I., Rauberg, J. & Tøffner-Clausen, L., 2014. The CHAOS-4 geomagnetic field model, *Geophys. J. Int.,* **197**(2), 815–827.

Olsen, N., Ravat, D., Finlay, C.C. & Kother, L.K., 2017. LCS-1: a high-resolution global model of the lithospheric magnetic field derived from CHAMP and Swarm satellite observations, *Geophys. J. Int.,* **211**(3), 1461–1477.

Olsen, N., Albini, G., Bouffard, J., Parrinello, T. & Tøffner-Clausen, L., 2020. Magnetic observations from CryoSat-2: calibration and processing of satellite platform magnetometer data, *Earth Planets Space,* **72** , doi:10.1186/s40623-020-01171-9.

Ott, E. *et al.*, 2004. A local ensemble Kalman filter for atmospheric data assimilation, *Tellus A,* **56**(5), 415–428.

Paek, H. & Huang, H.-P., 2012. A comparison of the interannual variability in atmospheric angular momentum and length-of-day using multiple reanalysis data sets, *J. geophys. Res.: Atmos.,* **117**(D20). doi: 10.1029/2012JD018105

Pais, M.A., Morozova, A.L. & Schaeffer, N., 2015. Variability modes in core flows inverted from geomagnetic field models, *Geophys. J. Int.,* **200**(1), 402–420.

Pedregosa, F. *et al.*, 2011. Scikit-learn: machine learning in Python, *J. Mach. Learn. Res.,* **12,** 2825–2830.

Pick, L., Korte, M., Thomas, Y., Krivova, N. & Wu, C.-J., 2019. Evolution of large-scale magnetic fields from near-Earth space during the last 11 solar cycles, *J. geophys. Res.: Space Phys.,* **124**(4), 2527–2540.

Raanes, P.N., Bocquet, M. & Carrassi, A., 2019. Adaptive covariance inflation in the ensemble kalman filter by Gaussian scale mixtures, *Q. J. R. Meteorol. Soc.,* **145**(718), 53–75.

Ropp, G., Lesur, V., Baerenzung, J. & Holschneider, M., 2020. Sequential modelling of the Earth's core magnetic field, *Earth Planets Space,* **72**(1), 1–15.

Sabaka, T.J., Hulot, G. & Olsen, N., 2010. Mathematical properties relevant to geomagnetic field modeling, in *Handbook of Geomathematics,* pp. 504–538, eds Freeden, W., Nashed, M. Z. & Sonar, T., Springer

Sabaka, T.J., Tøffner-Clausen, L. & Olsen, N., 2013. Use of the comprehensive inversion method for Swarm satellite data analysis, *Earth Planets Space,* **65**(11), 1201–1222.

Sabaka, T.J., Tøffner-Clausen, L., Olsen, N. & Finlay, C.C., 2018. A comprehensive model of the Earth's magnetic field determined from 4 years of Swarm satellite observations, *Earth Planets Space,* **70**(1), 1–26.

Sanchez, S., Wicht, J., Baerenzung, J. & Holschneider, M., 2019. Sequential assimilation of geomagnetic observations: perspectives for the reconstruction and prediction of core dynamics, *Geophys. J. Int.,* **217**(2), 1434–1450.

Sanchez, S., Wicht, J. & Bärenzung, J., 2020. Predictions of the geomagnetic secular variation based on the ensemble sequential assimilation of geomagnetic field models by dynamo simulations, *Earth Planets Space,* **72**(1), 1–20.

Schaeffer, N. & Jault, D., 2016. Electrical conductivity of the lowermost mantle explains absorption of core torsional waves at the equator, *Geophys. Res. Lett.,* **43**(10), 4922–4928.

Stephenson, F., Morrison, L. & Hohenkerk, C., 2016. Measurement of the Earth's rotation: 720 BC to AD 2015, *Proc. R. Soc. A: Math. Phys. Eng. Sci.,* **472**(2196), 20160404, doi: 10.1098/rspa.2016.0404

Taylor, J., 1963. The magneto-hydrodynamics of a rotating fluid and the Earth's dynamo problem, *Proc. R. Soc. A: Math. Phys. Eng. Sci.,* **274**(1357), 274–283.

Tibshirani, R., 1997. The lasso method for variable selection in the cox model, *Stat. Med.,* **16**(4), 385–395.

Walker, M.R. & Jackson, A., 2000. Robust modelling of the Earth's magnetic field, *Geophys. J. Int.,* **143**(3), 799–808.

Whaler, K.A. & Beggan, C.D., 2015. Derivation and use of core surface flows for forecasting secular variation, *J. geophys. Res.: Solid Earth,* **120**(3), 1400–1414.

APPENDIX A: DETERMINATION OF THE GRAPHICAL LASSO PARAMETER

Banerjee *et al.* (2008) showed that the parameter λ from eq. (29) can be chosen in order to minimize the probability of having false spurious correlations in the graphical model. Here the graphical model (that describes the dependence between model state parameters, seen as Gaussian random variables) is represented by the precision matrix Θ. Our goal here is to keep significant cross-covariances between the state variables while reducing the impact of noisy interactions (see Fig. 3), and having a reasonable evolution of the model uncertainties through time (avoiding ensemble collapse, see Fig. 4). This last criterion is nevertheless subjective, especially in our case where observational constraints vary with time.

In order to have a more objective criterion for the choice of the free parameter λ, we thus compute the likelihood for a given test set $\{\mathbf{z}\}$ as a function of λ, as explicitly described below. More precisely, we use k-fold cross-validation to find the λ value that maximizes the likelihood assuming a Gaussian distribution of the variance $P^f_{zz}(\lambda)$. The procedure to compute the optimal λ can be included in the algorithm and done at each analysis step, which would result in a completely adaptive algorithm. However, this would be computationally expensive and the gain would be small as in practice we find the optimal λ depends only weakly on time. It is mainly influenced by the number of realizations (see Fig. A1), and not much by others parameters. We therefore run the reanalysis with a chosen λ^*, and check in post-processing whether this value was optimal. We can say the value λ^* chosen for the reanalysis is optimal if it is equal to the λ returned by the cross-validation technique.

The first step of the k-fold cross-validation algorithm consists in selecting an ensemble of states $\left\{\mathbf{z}^j\right\}_{j\in[1\ldots N_e]}$ from a re-analysis at a given time t. For clarity, the dependence of the states $\left\{\mathbf{z}^j\right\}_{j\in[1\ldots N_e]}$ distribution on λ^* is not written explicitly. The following steps are then performed while varying the value of λ:

(1) $\left\{\mathbf{z}^j\right\}_{j\in[1\ldots N_e]}$ is partitioned in k sets $\{\mathbf{Z}^i\}_{i\in[1\ldots k]}$, each containing $N_{\text{test}} = N_e/k$ realizations.
(2) For each $i \in [1\ldots k]$:

(i) $\mathbf{Z}^i$ is considered as the test set, while the $N_{\text{train}} = (k-1)N_e/k$ remaining realizations constitute the training set $\mathbf{Z}^i_{\text{train}}$.
(ii) Compute the matrix $\hat{P}^f_{zz}(\lambda)$ from the training set $\mathbf{Z}^i_{\text{train}}$ and eqs (29,30).
(iii) For all $\mathbf{z}^j$ in the test set, the likelihood $L_{\delta\mathbf{z}^j}(\lambda)$ is then computed under the assumption of a multivariate Gaussian distribution:

$$L_{\delta\mathbf{z}^j}(\lambda) = \frac{1}{2\pi\,\det(\hat{P}^f_{zz}(\lambda))}\exp\left(-\delta\mathbf{z}^{j\,T}\hat{P}^f_{zz}(\lambda)^{-1}\delta\mathbf{z}^j\right). \tag{A1}$$

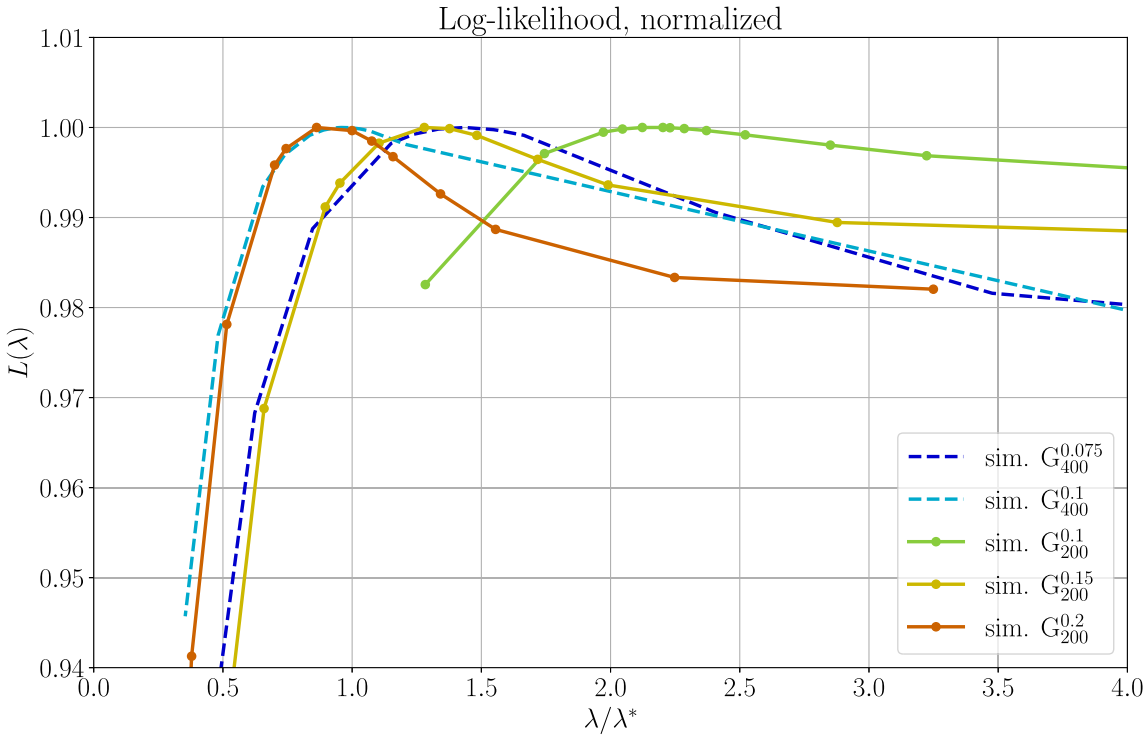

Figure A1. Normalized log-likelihood $(\langle L_{\lambda^*}\rangle + 2\max(\langle L_{\lambda^*}\rangle))/\max(\langle L_{\lambda^*}\rangle)$ as a function of λ/λ^*, for several values of λ^* and N_e. The estimation has been obtained at the epoch $t = 2019.08$ with forecast states, just before the analysis. Dotted (resp. dashed) lines correspond to cases with 200 (resp. 400) realizations. See the text for details.

(iv) Under a hypothesis of the independence of the ensemble of state increments $\delta \mathbf{z}^j$, the likelihood obtained knowing all realizations within the test sets is estimated as the product of the individual likelihood (A1), as

$$L_{\mathbf{Z}^i_{\text{test}}}(\lambda) = \prod_{\mathbf{z}^j \in \mathbf{Z}^i_{\text{test}}} L\left(\lambda | \delta \mathbf{z}^j\right). \tag{A2}$$

(3) We finally average the likelihood obtained from the k-test sets, to obtain

$$\langle L_{\lambda^*} \rangle (\lambda) = \frac{1}{k} \sum_{i=1}^{k} L\left(\lambda | \mathbf{Z}^i_{\text{test}}\right). \tag{A3}$$

Keeping the same sample, we perform this process for several values of the parameter λ until a maximum of the likelihood is found, giving an optimal value for λ. We represent in Fig. A1 the curves $\langle L_{\lambda^*} \rangle$ as a function of λ/λ^*. These have been normalized to their respective maximum-likelihood, because quantitative comparisons of the absolute likelihood level for the different sets of curves is not relevant as they were obtain under different configurations (in particular a different value of λ^*), implicitly underlying different hypotheses. We consider as an optimal choice for λ a situation where $\langle L_{\lambda^*} \rangle (\lambda)$ maximizes at $\lambda/\lambda^* = 1$, meaning that the posterior validation confirms the *a priori* choice for λ^*. The most important factor that controls the choice for λ is the number of realizations. We readily see that the best choice for λ is situated around the interval [0.15, 0.2] for $N_e = 200$, and [0.075, 0.1] for $N_e = 400$, indicating a scaling $\lambda \sim [30, 40]/N_e$.